Key Points:
- A 3-D density model of the greater Jan Mayen-East Greenland region was made based on crustal seismic, mantle tomography and gravity data
- A low-density anomaly deviates to the east from the Kolbeinsey Ridge across the West Jan Mayen Fracture Zone to the Mohn's Ridge
- The bottom lithospheric topography exerts a regional influence on upper asthenospheric flow driven northward by the Iceland plume

Correspondence to:
P. Tan,
pingchuan.tan@geo.uio.no

Lithospheric Control on Asthenospheric Flow From the Iceland Plume: 3-D Density Modeling of the Jan Mayen-East Greenland Region, NE Atlantic

Pingchuan Tan[1], Judith Sippel[2], Asbjørn Johan Breivik[1], Christian Meeßen[2], and Magdalena Scheck-Wenderoth[2,3]

[1]Centre for Earth Evolution and Dynamics, Department of Geosciences, University of Oslo, Oslo, Norway, [2]German Research Centre for Geosciences (GFZ), Potsdam, Germany, [3]Department of Geology, Geochemistry of Petroleum and Coal, RWTH Aachen University, Aachen, Germany

Abstract The density structure of the oceanic lithosphere north of Iceland is key for understanding the effects of the Iceland plume on the greater Jan Mayen-East Greenland Region. We obtain the 3-D density structure of the sediments and the crust from regional reflection and refraction seismic lines. The temperature and related density structures of the mantle between 50 and 250 km are derived from a shear wave velocity (Vs) tomography model. To assess the density between the Moho and 50-km depth, we combine forward and inverse 3-D gravity modeling. Beneath the Middle Kolbeinsey Ridge (MKR) region, a deep, broad negative mantle density anomaly occurs under the Kolbeinsey Ridge. It is overlain by a narrower uppermost mantle NE-SW elongated negative density anomaly, which is increasingly displaced eastward of the spreading axis northward. It crosses the West Jan Mayen Fracture Zone and becomes weaker approaching the Mohn's spreading ridge. The effect of this anomaly is consistent with significantly shallower basement on the eastern side of the MKR. We interpret this as the result of thermal erosion of the lithosphere by hot asthenospheric flow out from the Iceland plume, possibly the main driver for several eastward jumps of the MKR during the last 5.5 Ma. The cause for the deviation of the flow may be that the West Jan Mayen Fracture Zone is easier to cross in a region where the difference in lithospheric thickness is small. That implies that the bottom lithospheric topography exerts a regional but not local influence on upper asthenospheric flow.

1. Introduction

The Iceland plume exerts far-field effects on the thermal structure of adjacent mid-ocean ridges, both to the south (Reykjanes Ridge; e.g., Ito, 2001; Parnell-Turner et al., 2014; White et al., 1995) and to the north of the plume (e.g., Howell et al., 2014; Jones et al., 2002; Pilidou et al., 2005). There is debate as to what extent the spreading ridges channel the flow of plume material (e.g., Ito, 2001; Shorttle et al., 2010). Using observed seismic anisotropy patterns beneath Iceland, Xue and Allen (2005) suggest that there is a ridge-channelled flow of material away from Iceland toward the southern end of the Kolbeinsey Ridge. Based on a regional tomography model and observed gravity field, Marquart et al. (2007) pointed out that the Kolbeinsey Ridge is characterized by a large-scale radial buoyancy plume flux around Iceland, superimposed on the ridge perpendicular spreading. A later examination of geophysical and geochemical data along the Kolbeinsey Ridge, on the other hand, motivated Shorttle et al. (2010) to suggest that the Iceland plume spreads in a radial, pancake-like fashion. Recent high-resolution 3-D thermomechanical numerical modeling suggests that flow of the plume material along the Kolbeinsey Ridge is constrained by preexisting lithosphere structures related to the rifting of the Jan Mayen microcontinent off East Greenland (Koptev et al., 2017).

Several studies suggest that a lateral mantle flow related to the Iceland plume extends as far north as the West Jan Mayen Fracture Zone (WJMFZ; Breivik et al., 2008; Howell et al., 2014; Jones et al., 2002), shown by a sublithospheric low-velocity layer observed under the study area (Pilidou et al., 2005; Rickers et al., 2013). Similarly, the refraction seismic studies of Hooft et al. (2006) indicate that the Kolbeinsey Ridge (Figure 1) is characterized by shallow mantle melting caused by a hot and less viscous outflow of the Iceland plume into the asthenosphere under the ridge. Both regional geochemical and seismic studies suggest a decreasing
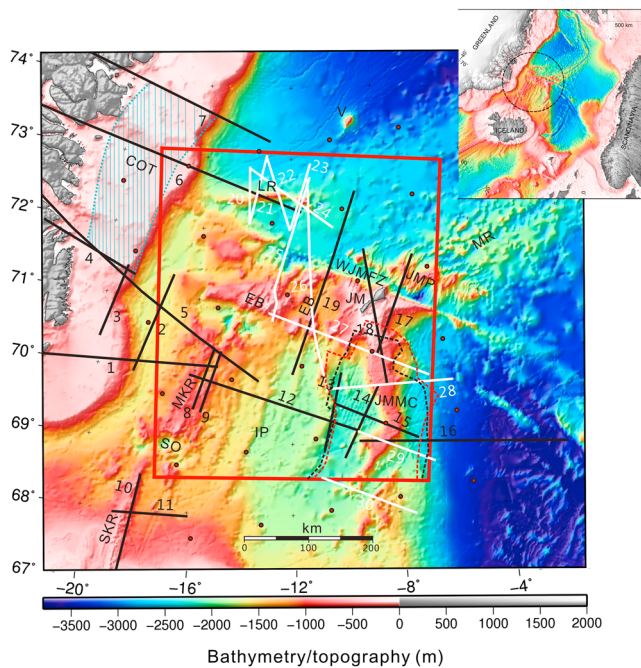
Figure 1. Topography and bathymetry of the study area (International Bathymetric Chart of the Arctic Ocean version 3; Jakobsson et al., 2012). Inserted map (ETOPO 2V2; National Geophysical Data Center, 2006) shows the location of the study area. The black and white lines show the locations of refraction and reflection seismic lines, respectively (annotations in Table 1). The Continent Ocean Transition Zone (COT) is shown in blue dotted lines (Hermann, 2013; Voss & Jokat, 2007), outline of the Jan Mayen Microcontinent (JMMC; black dashed line) is derived from Peron-Pinvidic et al. (2012a, 2012b), while the red dashed line represents the location of the JMMB by (Breivik, Mjelde, Faleide, & Murai, 2012) incorporating results from Kandilarov et al. (2012). The red dots represent points sampled from tomography model with a horizontal spacing of 100 km (Rickers et al., 2013). The Eggvin Bank is a topographically anomalous shallow area with scattered volcanic peaks between the Jan Mayen Island and East Greenland (Mertz et al., 2004). EB: Eggvin Bank, IP: Iceland Plateau, JM: Jan Mayen Island, JMP: Jan Mayen Plateau, JMMC: Jan Mayen Microcontinent, LR: Logi Ridge, MKR: Middle Kolbeinsey Ridge, MR: Mohn's Ridge, SO: Spar Offset, SKR: South Kolbeinsey Ridge, and V: Vesteris Seamount.

amount of thermal and geochemical plume influence with distance from the center of the Iceland plume (e.g., Hooft et al., 2006; Klingelhöfer, Géli, & White, 2000; Kodaira et al., 1997; Schilling, 1999).

The thermal structure of oceanic lithosphere is controlled by its cooling history so that temperature at a given depth decreases with increasing age and distance from a mid-ocean ridge (e.g., Adam & Vidal, 2010; Doin & Fleitout, 1996; Stein & Stein, 1992). The question is how the Iceland plume affects the thermal state of the greater Jan Mayen-East Greenland Region, where different segments of a number of active mid-ocean ridges meet (Figure 1). Haase et al. (2016) published 3-D forward and inverse gravity modeling of the NE Atlantic, where the temperature-dependent lithospheric mantle densities are derived from the age of the oceanic lithosphere following the approach of Sandwell (2001). We note that their model has a mass excess along the Kolbeinsey Ridge and north of the WJMFZ. This area correlates with an area of low upper mantle seismic S wave velocities (Rickers et al., 2013), which suggests that the upper mantle densities have been overestimated and that the gravity misfit in their model could be related to mass anomalies caused by the Iceland plume.

Measured gravity anomalies are the result of the density structure from the shallowest sediments, crust, and upper mantle. Information about the upper mantle density below 50 km can be derived from mantle tomography models, while the crustal structure and sediment distribution is reasonably well known from active source seismic data. We can use variations in the observed gravity field of the greater Jan Mayen-East Greenland Region to derive the density configuration of the upper mantle above 50 km to infer first-order trends of related temperature variations. The seafloor, the top of the basement (interface between sediments and crystalline crustal rocks), and the Moho (crust-mantle boundary) represent the largest density contrasts in the lithosphere. The region is relatively well covered by geological and geophysical observations derived from reflection and refraction seismic data (e.g., Hermann & Jokat, 2016; Kodaira et al., 1997, 1998a), teleseismics (e.g., Rickers et al., 2013), and gravity data (e.g., Gaina et al., 2011; Figure 1 and Table 1).

The objective of our study is to develop a 3-D density model of the study area that is consistent with all available geophysical observations to provide new constraints on the lateral geometry and extent of the shallowest upper mantle domain that is presently most affected by the Iceland plume.

2. Geological Setting

The research area extends from the Jan Mayen Ridge to the east coast of Greenland, and from the South Kolbeinsey Ridge in the south (Spar offset) to the Logi Ridge in the north (Figure 1). With the very slow spreading Kolbeinsey and Mohn's ridges (full spreading rate less than 20 mm/year; Gaina et al., 2009), the anomalously shallow Eggvin Bank, the Jan Mayen Microcontinent (JMMC), and the tectonically active WJMFZ, the region represents one of the most complex areas of the NE Atlantic region.

The rifting of the JMMC off the East Greenland margin occurred around 24–25 Ma due to the spreading axis jump from the Aegir Ridge to the Kolbeinsey Ridge (e.g., Nunns, 1982). The spreading along the Kolbeinsey Ridge is slow (full rate: 16–18 mm/year) and nearly orthogonal (Appelgate, 1997). It underwent several minor eastward jumps of the spreading axis (e.g., Appelgate, 1997). The Kolbeinsey Ridge is divided into three different sections (southern, middle, and northern parts), of which the study area only covers the middle and northern parts. The Middle Kolbeinsey Ridge (MKR) and surrounding Iceland Plateau show abnormally thick oceanic crust (average 9 km) and shallow bathymetry (Kodaira et al., 1997, 1998b), which is attributed to the thermal influence of the Iceland plume (Elkins et al., 2011; Kodaira et al., 1997, 1998a, 1998b). The MKR basalts are related to a homogeneously depleted mantle source (e.g., Elkins et al., 2011). In contrast, the basalts

Table 1
Database for the Construction of a 3-D Structural and Density Model That Differentiates the Main Sedimentary and Crustal Units

Input regional seismic reflection and refraction lines

Label (Figure 1)	Line name	Reference	Available information
1–4	ARK 1988 lines 3–6	Weigel et al. (1995)	V_p model, 2-D gravity
5	AWI20090100	Hermann (2013)	V_p model, 2-D gravity
6–7	AWI20030400 and AWI 20030500	Voss and Jokat (2007)	V_p model, 2-D gravity
8–9	JMKR-95 lines 1–2	Kodaira et al. (1997) and Mjelde et al. (2002)	V_p model, V_s model
10	KRISE line 1	Hooft et al. (2006)	V_p model, 2-D gravity, isostasy
11	KRISE line 4	Furmall (2010)	V_p model
12	JMKR-95 lines 3	Kodaira et al. (1998b) and Mjelde et al. (2002)	V_p model, V_s model
13–15	JMKR-95 lines 4–6	Kodaira et al. (1998a) and Mjelde et al. (2007)	V_p model, V_s model, 2-D gravity
16	OBS 2000 lines 8–00	Breivik, Mjelde, Faleide, and Murai (2012)	V_p model
17–18	OBS-JM-2006 lines 1–2	Kandilarov et al. (2012, 2015)	V_p model, V_s model, 2-D gravity
19	Profile 1	Tan et al. (2017)	V_p model, V_s model
20–24	Profile 2–6	Breivik, Mjelde, Rai, and Frassetto (2012)	Reflection seismic
25–27	NPDJM11-004,005,006	Sandstå et al. (2012)	Reflection seismic
28–30	NPD08, Inseis 01, Inseis 06	Peron-Pinvidic et al., (2012a, 2012b)	Reflection seismic

Additional constraints

Name	Reference	Comments
Crustal models of the Mohn's Ridge	Klingelhöfer, Géli, Matias, et. al. (2000) and Klingelhöfer, Géli, and White (2000)	Constrain the Moho depth in the Mohn's Ridge for oceanic ages less than 22 Ma (Figure 2c)
Moho depth of NE Atlantic	Haase et al. (2016)	Derived from 3-D gravity inversion modeling; here only used in the NKR where refraction seismics are lacking (Figure 2c)
Sediment thickness of world's ocean and marginal seas	Divins (2004)	Grid spacing of 5 arc min by 5 arc min provides additional information on the depth of the basement
CRUST 1.0	Laske et al. (2013)	1 × 1° grid provides additional information on the depth of Moho

from the North Kolbeinsey Ridge (NKR) and nearby Eggvin Bank are enriched in incompatible elements and radiogenic isotopic composition (e.g., Elkins et al., 2016; Haase et al., 2003). The Eggvin Bank is a shallow region surrounding the northern Kolbeinsey Ridge segment. A seismic refraction line across the bank approximately 70 km east of the spreading ridge shows large variations in crustal thickness (from 8 to 13 km; Tan et al., 2017). The seismic velocities indicate that there could be some thermal Iceland plume influence under the northern Eggvin Bank, while the elevated magmatism in the southern Eggvin Bank may be mostly affected by an enriched mantle source (Tan et al., 2017).

The WJMFZ offsets the adjacent spreading axes right laterally by about 200 km. North of the fracture zone, opposite of the Jan Mayen Island (Figure 1), spreading takes place on the Mohn's Ridge. The formation of the Mohn's Ridge dates back to the continental breakup between Greenland and Norway in the Early Eocene (54–55 Ma). The rate of spreading is symmetrical having a full rate of 16 mm/year, and the spreading direction is moderately oblique. It is mostly producing a thin oceanic crust (4 $\pm$0.5 km; Kandilarov et al., 2012; Klingelhöfer, Géli, & White, 2000; Klingelhöfer, Géli, Matias, et al., 2000). The thick oceanic crust observed along the East Greenland and conjugate Norwegian margins show that the commencement of the Mohn's Ridge was influenced by the Iceland plume to increase magma productivity during the earliest spreading phase (e.g., Breivik et al., 2009, 2014; Voss & Jokat, 2007).

The JMMC has large crustal thickness variations. The maximum thickness is observed at the northern boundary of the JMMC (25 km), while the minimum could be as low as 3 km (Kandilarov et al., 2012; Kodaira et al., 1998a). In addition, the eastern and western sides of JMMC are interpreted as volcanic and nonvolcanic rifted margins, respectively (e.g., Breivik, Mjelde, Faleide, Murai, 2012; Kodaira et al., 1998a).

3. Three-Dimensional Gravity Modeling

3.1. Modeling Strategy

Aside from one refraction seismic profile (Hermann & Jokat, 2016), there is a lack of seismic constraints on mantle densities between 50 km (below sea level) and the Moho. Hence, the main purpose of performing 3-D gravity modeling is to close this observation gap between the crust and mantle densities that can be obtained from mantle tomography. Therefore, we integrate the data-derived densities for the sediments, crust, and deeper mantle into an initial 3-D density model and adjust the 3-D density configuration of the shallowest mantle until the gravity response of the entire 3-D model is consistent with the observed gravity anomalies.

First, we calculate the gravity response of an initial 3-D density model that includes the data-constrained densities of the sediments, crust, and deeper mantle, while including a constant density of 3,300 kg/m^3 for the shallowest unconstrained mantle (forward gravity modeling). As a result of this step, we obtain the gravity misfit of this initial 3-D density model by subtracting the observed gravity from the calculated gravity. A positive gravity misfit then corresponds to a mass excess in the model. In a second step, we use the gravity misfit to invert for the density configuration of the shallowest mantle above 50 km depth (inverse gravity modeling).

For the forward calculations, we use the Interactive Gravity and Magnetic Application System IGMAS+ (Götze & Lahmeyer, 1988; Schmidt et al., 2011; Schmidt & Götze, 1998). IGMAS+ calculates the total gravity response of a predefined 3-D density model by combining triangulated model geometries (polyhedrons that geometrically define geological units) with density information attached to voxel cubes. For the inverse gravity modeling step, we make use of a modified version (Meeßen et al., 2018) of the Harvester module (Uieda & Barbosa, 2011), which is part of the open-source code library *fatiando a terra* (for Python 2.7; Uieda et al., 2013).

3.2. Modeling the Structure and Density of the Sediments and Cystalline Crust

Previous studies, including (i) the interpretation of reflection seismic data (Blischke et al., 2016; Peron-Pinvidic et al., 2012a, 2012b), (ii) wide-angle refraction seismic data (Breivik, Mjelde, Faleide, Murai, 2012; Hermann & Jokat, 2016; Kandilarov et al., 2012, 2015; Klingelhöfer, Géli, & White, 2000; Klingelhöfer, Géli, Matias, et. al., 2000; Kodaira et al., 1997, 1998b; Tan et al., 2017; Voss & Jokat, 2007; Weigel et al., 1995), and (iii) studies of dredged samples (e.g., Elkins et al., 2011, 2016; Haase et al., 2003; Klingelhöfer, Géli, & White, 2000; Mertz et al., 2004; Schilling, 1999), show that the study area is characterized by large variations in terms of crustal structure as well as mantle composition, and mantle melting degree. Table 1 and Figure 1 provide an overview of the data types and sources used to develop a 3-D structural and density model for the crystalline crust and sedimentary cover. Based on the published interpretations, we define 10 sedimentary and crustal layers with characteristic densities for our study area (left column of Table 2) and thus be used to construct the elements for the 3-D density model.

Table 2
Densities of Geological Units From Publications Used to Setup the Initial 3-D Density Model (Last Column)

	Voss & Jokat 2007 East Greenland (Logi Ridge)	Weigel et al. 1995 East Greenland (MKR)	Peron-Pinvidic et al., 2012a, 2012b JMMC	Mjelde et al. 2007 JMMC, Iceland Plateau	Kandilarov et al. 2012 JMMC, Jan Mayen	Hooft et al. 2006 SKR	Hermann 2013 NE Atlantic (3-D modeling)	Haase et al. 2016 NE Atlantic (3-D modeling)	Modeled Density (kg/m³)
	Density (kg/m³) published for the surrounding area								
Water	1,030	1,030	1,030	1,030	1,030	1,030	1,030	1,030	1,030
Cenozoic upper	2,000–2,400	2,100	2,100	2,000	2,200		1,900–2,100	2,200	2,100
Cenozoic lower	2,330–2,520		2,100	2,300	2,400		2,400	2,200–2,700	2,400
Precenozoic	2,560–2,650	2,300–2,600	2,560	2,520–2,730	2,400			2,200–2,700	2,650
Upper oceanic crust	2,600	2,800–2,900	2,750	2,840		2,850	2,900	2,850	2,700
Lower oceanic crust	2,900	3,000–3,100	3,000	3,000		2,850	2,900	2,850	3,000
Upper continental crust	2,720		2,740	2,700–2,820	2,750–2,950		2,700	2,750	2,700
Lower continental crust	2,830–2,900		2,950	2,830–2,960	3,050		2,950	2,950	2,950
Lower-crustal intrusions	3160						3,180		3,160
Upper crust (JMMC)					2,900			2,950	2,900
Lower crust (JMMC)					3,050			2,950	3,050
Upper mantle	3,240–3,310	3,200–3,300	3,300		3,200–3,400	3,240	3,220–3,310	3,200–3,300	

Note. MKR = Middle Kolbeinsey Ridge; JMMC = Jan Mayen Microcontinent; SKR = South Kolbeinsey Ridge.
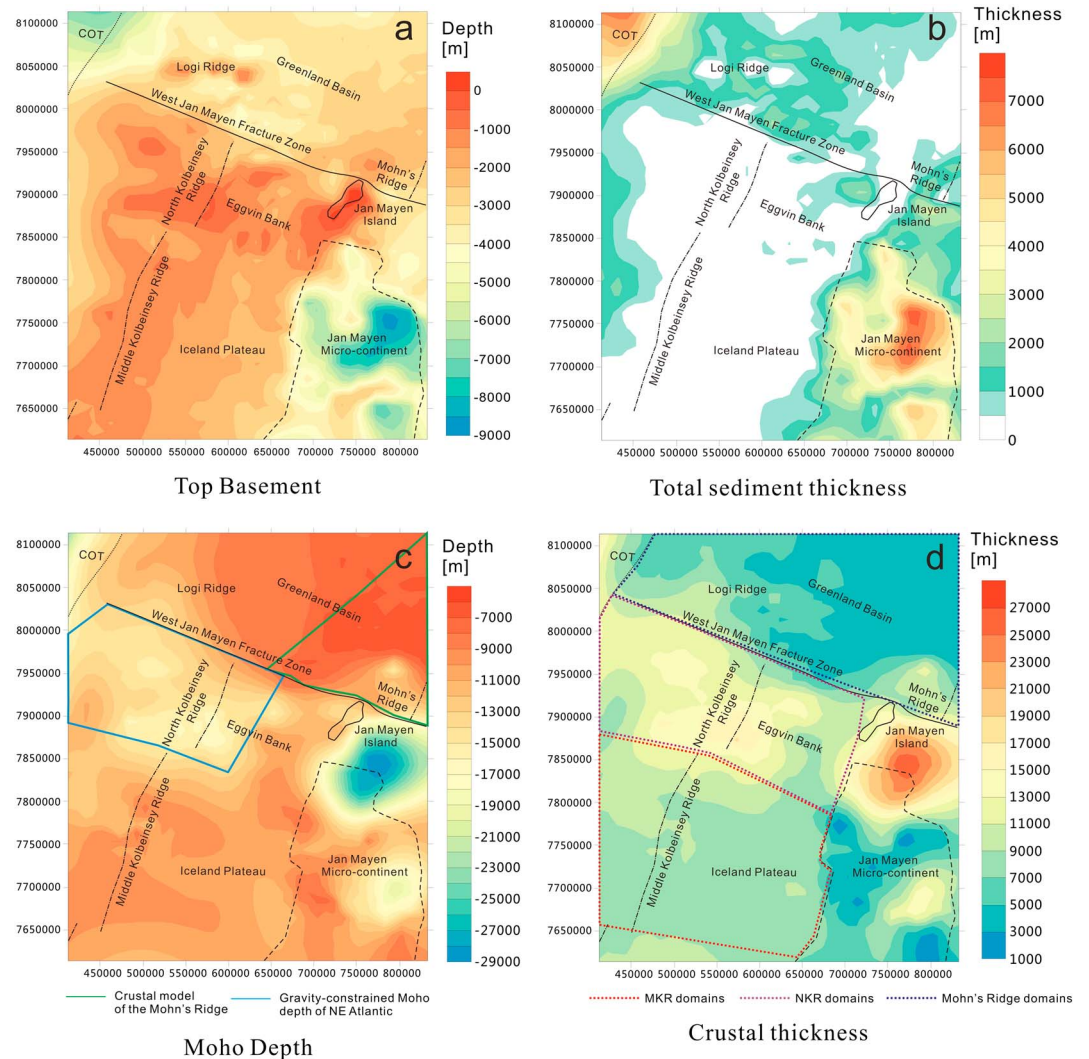
Figure 2. Major structural elements of the crust. Locations of three present-day spreading axis are derived from regional magnetic anomaly data (Olesen et al., 2007). (a) Depth to the top of the crystalline crust (basement). (b) Total sediment thickness. (c) Depth to the crust-mantle boundary (Moho) as mostly constrained by seismic data (Figure 1), the area constrained by the crustal model of the Mohn's Ridge (Klingelhöfer, Géli, Matias, et. al., 2000) and gravity-constrained Moho depth of the NE Atlantic (Haase et al., 2016) are presented by green and blue lines, respectively. (d) Thickness of the crystalline crust; the color-coded dotted lines outline three different domains (Middle Kolbeinsey Ridge (MKR), North Kolbeinsey Ridge (NKR), and Mohn's Ridge) used for further analysis (see main text).

The Cenozoic sediments are dominated by muds and silts with some additional ice-rafted material from the recent glacial periods (e.g., Blischke et al., 2016; Haase et al., 2003; Thiede & Hempel, 1991). At depths down to 1 km they are estimated to have low densities (2,100 kg/m^3); higher densities (2,400 kg/m^3) were assigned to deeper Cenozoic sediments (burial greater than 1 km). The pre-Cenozoic sediment layers, which are only observed in the JMMC, are characterized by relatively high velocities (4.5–5.6 km/s) and thus are modeled with the highest sedimentary densities (2,650 kg/m^3).

The oceanic crust is divided into two layers, a lower-velocity upper crust (V_p: 2.5–6.6 km/s) and a high-velocity lower crust (V_p: 6.6–7.6 km/s). The upper oceanic crust corresponds to pillow lavas and sheeted dikes (Detrick et al., 1994; Dilek, 1998). It is strongly influenced by fissures and cracks causing higher porosity (Jacobson, 1992); thus, it was assigned lower densities (2,700 kg/m^3). The lower crust is characterized by gabbroic rocks of low porosity and higher density (3,000 kg/m^3). Dense intruded bodies (3,160 kg/m^3) are indicated by regional refraction studies in the area of the Greenland continental-ocean transition (Figure 1; Hermann, 2013; Voss & Jokat, 2007).

The continental crust of the JMMC is divided into an upper layer of lower V_p (4.5–6.5 km/s) and modeled density (2,700 kg/m^3) and a lower layer of higher V_p (6.5–6.85 km/s) and density (2,950 kg/m^3). A relatively dense upper (2,900 kg/m^3) and lower crust (3,050 kg/m^3) is restricted around the northern boundary of the JMMC where the Moho depth is greatest (Kandilarov et al., 2012, 2015).

The modeled crustal densities are consistent with empirical velocity-density relationships (Barton, 1986) and are within the range of densities from previous studies (Table 2). The Moho depth is mainly constrained by seismic lines revealing mantle refractions (P_n) and Moho reflections (P_mP). It represents an intralithospheric boundary with a large density contrast, which is characterized by an increase in P wave velocity to values greater than 7.6 km/s.

We used QGIS (QGIS Devlopment Team, 2009) to georeference all the seismic constraints into a consistent coordinate system (UTM 28N). Since seismic profiles do not cover the entire area, we have implemented additional constraints (Table 1). These are (i) a crustal model of the Mohn's Ridge (Greenland Basin) covering the region of oceanic ages of less than 22 Ma (Klingelhöfer, Géli, & White, 2000); (ii) Moho depths of the NE Atlantic as derived by 3-D gravity inversion (Haase et al., 2016), which were only used in the western NKR domain where refraction seismic data are lacking; (iii) a global model of oceanic sediment thickness (Divins, 2004); and (iv) crustal thickness (CRUST 1.0; Laske et al., 2013; Table 1 and Figure 2c). These models provide additional information on the depth of basement and the Moho, which we use to fill the gaps between the original seismic constraints.

The results from seismic lines and additional constraints listed in Table 1 were jointly interpolated with Petrel (by Schlumberger 1998–2013) using the Minimum Tension Gridding algorithm to create regular grids of interfaces. In case of the WJMFZ, due to the sharp changes across the fracture zone, we first interpolate between seismic lines north of the WJMFZ to create regular grids, then we interpolate between seismic lines south of the WJMFZ, and finally, we combine these two grids together. The dimensions of the final modeling area are 420 km in north-south direction and 500 km in east-west direction. The model has a horizontal node spacing of 10 km in both northing and easting directions. The vertical spacing (down to Moho depth) corresponds to the thickness of the different geological units. The chosen model node spacing preserves the main structural trends derived from the seismic refraction and reflection lines.

Figure 2 shows the two key horizons (top basement and Moho), as well as sediment and crustal thickness. The basement depth in the oceanic domain increases with increasing distance from the spreading centers (Figure 2a). In addition, wide parts of the Kolbeinsey Ridge, Iceland Plateau, and Eggvin Bank are high standing areas. Here the depth of the basement is almost equal to the seafloor bathymetry, while a thin layer of sediments (< 2 km) is observed in the western domain of the MKR. In the Greenland Basin (north of the WJMFZ), the sediments are only Cenozoic with a thickness of less than 500 m around the Mohn's spreading ridge, increasing to 7,000 m toward the continent-ocean boundary off Greenland (Figure 2b). The JMMC is covered by sediments varying in thickness from 0 to 7000 m (Figure 2b). The sedimentary section is thickest along the eastern margin of the JMMC (Figure 2b).

In the Greenland Basin, the Mohn's Ridge shows a shallow Moho depth of approximately 7 km, while the Moho depth increases to 19 km toward the continent-ocean boundary off Greenland (Figure 2c). The average crystalline crustal thickness is around 8.5 km along the MKR and adjacent Iceland Plateau, and increases to around 12–15 km over the Eggvin Bank in the NKR domain (Figure 2d). In the JMMC, the Moho depth varies strongly with the shallowest depths beneath the western edge of the JMMC (Jan Mayen Basin; 8.5 km), moderate depths beneath the eastern edge of the JMMC (Jan Mayen Ridge; 18 km), and largest depths around the northern part of the JMMC (27 km; Figure 2d). The western margin of the JMMC shows an abrupt transition from thin continental crust (5 km) to a thick oceanic crust (9 km) in the Iceland Plateau (Figure 2d).

3.3. Density Configuration of the Mantle at Depths Below 50 km (Below Sea Level)

The seismic wave velocity configuration of the mantle provides constraints on its thermal and hence density structure, although the proposed methods of wave velocity conversion differ significantly (Cammarano & Guerri, 2017). For the greater Jan Mayen-East Greenland Region, the velocity of horizontally polarized shear waves (V_{SH}) in the mantle can be derived from a tomographic model of the North Atlantic region (Rickers et al., 2013). It is based on nonlinear full-waveform inversion techniques and measurements of the instantaneous phase misfit. Compared to the global S wave model S20RTS (Ritsema et al., 1999) and European full-waveform model (EU-TF; Fichtner & Trampert, 2011), the V_{SH} model (NA-IP; Rickers et al., 2013) is characterized by a signif-
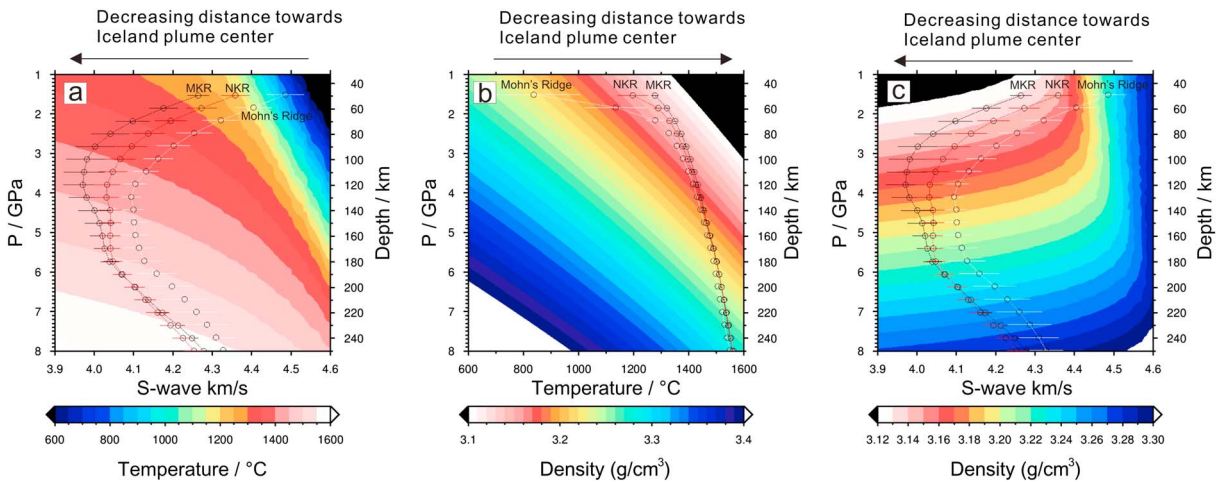
Figure 3. (a) Temperature field calculated by using the conversion of Priestley and McKenzie (2006). (b) Results of density calculation (equation (1)– (5)) applied to pressure and temperature ranges of 1 to 8 GPa and 600 to 1600 °C. (c) Calculated density as a function of the pressure and S wave velocity variations. Superimposed circles and bars represent the parameter variation obtained from subdomains of the study area; the horizontal bars indicate the standard deviation of V_s (Figures 3a and 3c) and temperature (Figure 3b), while the mean is indicated by the circles. The black, red, and white lines show the data derived from Middle Kolbeinsey Ridge (MKR), North Kolbeinsey Ridge (NKR), and Mohn's Ridge domains (Figure 2d), respectively.

icantly improved resolution for both the upper and lower mantle; therefore, it images small-scale anomalies, such as spreading ridges and plume distribution under the NE Atlantic Region. The V_{SH} model comes with a horizontal grid spacing of 100 km and a depth-dependent vertical spacing of 10 km in the uppermost 350 km, 20 km between 350 and 700 km, and 50 km between 700- and 1,300-km depth. Given the vertical grid size of the V_{SH} tomography (10 km) at shallow depths and the maximum Moho depth > 28 km (Figure 2c), we suggest that the values of V_{SH} shallower than 50 km are likely to be artificially affected by the crustal velocities. In addition, compared to the V_{SH} constraints at greater depth (e.g., 100 km), the mantle between the Moho and 50 km is more likely represented by lithospheric mantle compared to asthenospheric mantle. Therefore, we restrict the usage of V_{SH} constraints to depths >50 km for 3-D gravity modeling. First, we convert the regional V_{SH} tomography model into mantle temperature. Then, the mantle density can be estimated as a function of pressure and temperature.

3.3.1. Conversion of Shear Wave Velocity to Temperature

Based on an averaged shear wave velocity model and a generic thermal model for the Pacific oceanic lithosphere, Priestley and McKenzie (2006) proposed a set of empirical equations and constants to convert mantle shear wave velocity to temperature (*T*). The conversion method is based on the assumption that the shear velocity structure of the oceanic upper mantle can be largely explained by its temperature, pressure, and some activation processes that are related to an elastic behavior close to melting temperatures. Retained melt present at low concentration is expected to have a minor impact. Hence, this nonlinear V_s-*T* relationship is assumed to be valid for any mantle composition, while being most accurate for temperatures that exceed 1100 °C.

For the V_s-*T* conversion, the original *S* wave model has been extracted for the depth range of 50–250 km. The V_s model has been rescaled by applying the Triangulation Method of the software OpendTect (Huck, 2012) to create a regular grid with 10×10 km horizontal and 10 km vertical dimension. This node spacing is consistent with the upper crustal and sedimentary model. One variable to be predefined for the empirical equations to be solved is pressure (Priestley & McKenzie, 2006). In this study, we use sedimentary and crustal density structures (Table 2) and an assumed constant mantle density (3,300 kg/m³) to estimate the corresponding pressure variations. Figure 3a shows the temperature configuration derived from the entire tomographic model in the parameter space of V_{SH}, depth, and pressure. In general, the converted temperature is increasing as the depth increases and velocity decreases, but lateral temperature differences are much larger at shallow depths.

The V_s-to-*T* conversion is a strongly nonlinear function of temperature and the uncertainties of the temperature estimates decrease with increasing temperature (Priestley & McKenzie, 2006, 2013). As proposed by Priestley and McKenzie (2013), V_s-derived temperatures below 900 °C are associated with large uncertainties,

where a change in V_s of 0.04 km/s would result in a 250 °C difference. The same V_s change at 1200 °C would correspond to 100 °C and at 1350 °C, it would only be 30 °C (Figure 3a).

3.3.2. Conversion of Temperature to Density

The density of the mantle is controlled by its composition and the in situ pressure and temperature conditions. Throughout this modeling study, we assume that the mantle of the greater Jan Mayen-East Greenland Region is compositionally homogeneous. Bai et al. (2014) have proposed a set of equations to calculate the density of mantle rock at given pressure and temperature. Thereby, both the thermal expansion coefficient (α_T) and the bulk modulus (K_T) are considered as temperature dependent, while the authors derive their formulation from laboratory measurements on olivine samples as described by Kroll et al. (2012), which is based on a large number of thermal expansivity measurements and an up-to-date summary of bulk modulus data. The mantle density affected by thermal expansion at temperature T is

$$\rho_T = \rho_0[1 - \alpha_T(T - T_0)] \tag{1}$$

where T_0 is equal to 273 K, while ρ_0 is the mantle reference density (3,300 kg/m³) at temperature T_0. The relationship between α and T is estimated by Bai et al. (2014) with a nonlinear function of temperature:

$$\alpha_T = (6 \times 10^{-10}T^3 - 2 \times 10^{-6}T^2 + 0.0039T + 1.727) \times 10^{-5} \tag{2}$$

The bulk modulus K represents the pressure change required for a given volume change. The bulk modulus can be calculated as a function of temperature (Kroll et al., 2012):

$$K_T = 127.97 - 0.0232(T - 300) \tag{3}$$

where the units for K_T and T are gigapascal and kelvin, respectively.

The density changes related to the in situ pressure ($\Delta\rho_p$) at a specific pressure (P) and bulk modulus (K) can be calculated using the following function (Bai et al., 2014):

$$\Delta\rho_p = \rho_0[P - P_0]/K_T \tag{4}$$

where P_0 is the standard atmospheric pressure and the unit for P is gigapascal.

Finally, the mantle density for a specific temperature and pressure is calculated:

$$\rho = \rho_T + \Delta\rho_p \tag{5}$$

Figure 3b shows the density variation for pressure and temperature ranges of 1 to 8 Gpa and 600 to 1600 °C, respectively. At a given depth, high mantle temperature corresponds to lower mantle density, while at a given temperature, the larger the pressure (greater depth) the higher the corresponding mantle density. Under a specific temperature and pressure, the modeled mantle density reveals similar results compared to mantle densities based on Grose and Afonso (2013) and Schutt and Lesher (2006) using the same reference mantle density (3,300 kg/m³).

3.3.3. Results

Figure 3c shows the calculated mantle density variation as a function of the pressure and V_s variations. For most of the parameter field, density increases with depth. At depths shallower than 90 km, the mantle densities reveal large lateral variations due to large variations in mantle temperature (Figure 3a). The calculated mantle density range at 50-km depth is 151 kg/m³ (3,127–3,278 kg/m³), decreasing to 10 kg/m³ (3,145–3,155 kg/m³) at 90-km depth. The mantle densities at depths greater than 90 km have a range of less than 10 kg/m³ (Figure 3b).

The MKR, NKR, and Mohn's Ridge show significantly different V_s, mantle temperature, and density configurations (Figure 3), in particular at depths shallower than 90 km. At a given depth, MKR has the lowest V_s, correspondingly highest mantle temperature, and lowest mantle density. In contrast, the Mohn's Ridge shows the highest V_s, lowest mantle temperature and largest mantle density.

Figure 3b shows that under the MKR domain, the thermal gradient is decreasing with increasing depth. At shallower depth (<90 km), the average thermal gradient is 2.5 K/km. At depths >90 km, thermal gradients decrease to an almost constant value around 0.8 K/km. The mantle densities at MKR are characterized by small changes (3,130 to 3,140 kg/m³) at depth shallower than 90 km, which indicates that the temperature and pressure effects nearly compensate each other. At depths >90 km, the mantle density is mainly influenced by the pressure as it is gradually increasing with a constant density gradient of around 1 kg/m³/km.
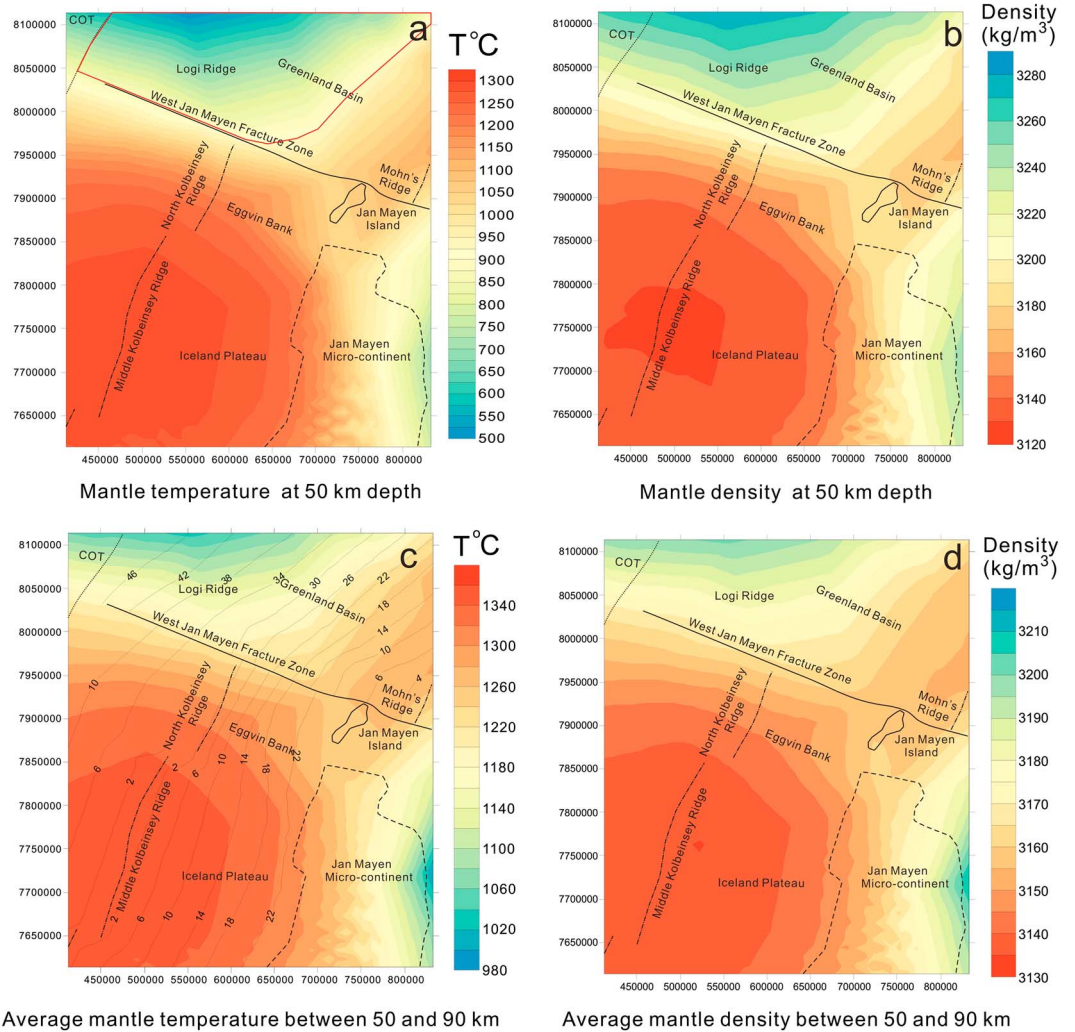
Figure 4. (a) Converted temperature variations at a depth of 50 km. The red solid line delineates an area within the Greenland basin with temperatures of less than 900 °C. (b) Corresponding density variations at a depth of 50 km. (c) Average mantle temperature between 50 and 90 km (T_{50-90}). The solid gray lines with numbers show the oceanic seafloor ages (Müller et al., 2008). (d) Average mantle density between 50 and 90 km (ρ_{50-90}). COT = Continent Ocean Transition Zone.

The mantle temperature below Mohn's Ridge is characterized by a significantly higher thermal gradient (>20 K/km) at depths between 50 and 70 km. However, where depths exceed 70 km, the thermal gradient is similar to the MKR. Under the Mohn's Ridge, the average mantle density is decreasing from 3,230 kg/m³ (50-km depth) to 3,150 kg/m³ (70-km depth; Figure 4b). At depths larger than 70 km, the mantle density is gradually increasing (1 kg/m³/km) as the pressure plays a more significant role to determine the mantle density. At a given depth, the average mantle temperature and density of the NKR domain are between those of the MKR and Mohn's Ridge.

As the largest lateral temperature and density variations are observed for depths between 50 and 90 km, we plot the average mantle temperature (T_{50-90}) and density (ρ_{50-90}) for this depth interval (Figures 4c and 4d). In general, this interval shows trends of decreasing T_{50-90} (increasing ρ_{50-90}) from MKR to NKR and to Mohn's Ridge, and each ridge also shows similar trends of decreasing temperature (increasing density) with increasing age of the oceanic crust. For example, under the MKR domain, T_{50-90} is 1350 °C under the ridge axis and gradually decreases to 1310 °C at locations where the oceanic crust is as old as 22 Ma. Under the Mohn's Ridge, the mantle temperature at the spreading center is 1270 °C, while it decreases to 1050 °C at around 45 Ma. In contrast to the MKR and Mohn's Ridge, the mantle temperature and density under the NKR domains have large variations, where the mantle temperature decreases (density increases) northward.

3.4. Gravity Response of the Initial 3-D Density Model

In order to avoid edge effects during the gravity modeling, we have extended the model horizontally by 300 km in all directions. The extended area is mainly constrained by regional seismic refraction studies (Brandsdóttir et al., 2015; Furmall, 2010; Hermann, 2013; Hooft et al., 2006; Klingelhöfer, Géli, & White, 2000; Voss & Jokat, 2007; Weigel et al., 1995; Figure 1), the global map of oceanic sediment thickness (Divins, 2004), and the model CRUST 1.0 (Laske et al., 2013).

We performed the gravity modeling covering an area of 1,020 × 1,100 km (extended region) for the density configurations of the sediments, crust, and mantle above 250 km (regular 10-km × 10-km grids). The 3-D density model in IGMAS+ is built upon a series of parallel vertical 2-D planes, where the 3-D structure is obtained by triangulating polyhedrons between planes. In this study, the gravity model contains 56 parallel working planes running in east-west direction at 20-km intervals. Thus, the 2-D planes are approximately perpendicular to the mainly N-S directed major structural elements, crossing the most important gravity lows and highs (Figure 5a).

To each sedimentary and crustal model unit, a homogeneous density is assigned (Table 2). The mantle density is constant (3,300 kg/m^3) between the Moho and 50 km, while the S wave-derived density configuration of the mantle between 50- and 250-km depth is modeled by a voxel grid with a regular spacing of 10 km in both horizontal and vertical directions.

The gravity field data that we have chosen to use is CAMP-G (Gaina et al., 2011), a recently published Arctic gravity field model (10- × 10-km grid resolution) containing free-air gravity anomalies offshore and Bouguer anomalies onshore (Jan Mayen Island; Figure 5a). It is an expansion of the ArcGP free air gravity published by Kenyon et al. (2008) by compiling regional gridded data and merging that with a hybrid satellite-/surface measurement-based gravity model (EIGEN GL04C; Förste et al., 2008) for the long wavelengths. There is a gravity low over the eastern margin of the JMMC and Jan Mayen Basin. The gravity field over the Eggvin Bank, Jan Mayen Island, and Jan Mayen Ridge show pronounced high gravity. In addition, the WJMFZ is characterized by a narrow gravity low bounded by positive gravity anomalies on both sides. The gravity over most parts of the Mohn's Ridge and the MKR reveal moderately positive anomalies, ranging from 20 to 40 mGal.

Figure 5c shows the gravity misfit (root-mean-square, RMS: 34.24 mGal) calculated as the gravity response of the initial density model (Figure 5b) minus the observed gravity (Figure 5a). Any negative gravity misfit implies a mass deficit in that particular area of the model. The initial gravity misfit is characterized by a NE-SW striking, positive (up to 60 mGal) misfit trending from MKR to the Mohn's Ridge. At MKR, this anomaly runs slightly east from the spreading axis, where the gravity misfits are gradually decreasing away from this trend. The JMMC is dominated by short-wavelength negative misfits, while short-wavelength positive misfit anomalies are observed at the Eggvin Bank. In addition, we calculated gravity response induced by masses located above the Moho (Figure 5d) and mantle below 50 km (Figure 5f), and their corresponding gravity misfit anomaly fields (Figures 5e and 5g), in order to reveal how they contributed to the gravity modeling.

3.5. Gravity Inversion: Mantle Density Shallower Than 50 km

The gravity misfit calculated for the initial 3-D density model (Figure 5c) provides the boundary condition for the inversion step: To minimize the gravity misfit of the forward model, we use the Harvester algorithm (Uieda & Barbosa, 2011; Uieda et al., 2013) to stepwise modify the density distribution of the mantle at depths <50 km. This algorithm propagates initial density perturbations—the *seeds*—through a mesh of rectangular prisms with a defined reference density—the *medium*—repeated until the corresponding forward gravity field reaches the prescribed boundary condition. In the present study, the seeds initially form a 1-km-thick layer of which (i) the base is situated at a depth of 50 km and (ii) the density distribution is equal to the one at 50-km depth as derived from the V_{SH} constraints (Figure 4b). The minimum top depth is constrained by the Moho. The seeds replace the medium in the upward direction, where the medium is assigned a constant density of 3,300 kg/m^3 (a mantle density value typical at the depth of the Moho). The final thicknesses of the seeds and the medium (obtained when the gravity misfit is minimized) define the average bulk density of the shallowest mantle. Hence, we have calculated the vertically averaged density of the mantle at depth of <50 km, by weighting the density of a seed and its overlying medium by their relative thicknesses for each column:

$$\rho_{\text{average}} = (t_m \cdot 3,300\text{kg/m}^3 + t_s \cdot \rho_s)/(t_m + t_s) \tag{6}$$

where ρ_{average} and ρ_s represent the average mantle density at depths shallower than 50 km and the density of seeds, while the t_m and t_s corresponds to the thickness of medium and seeds, respectively.
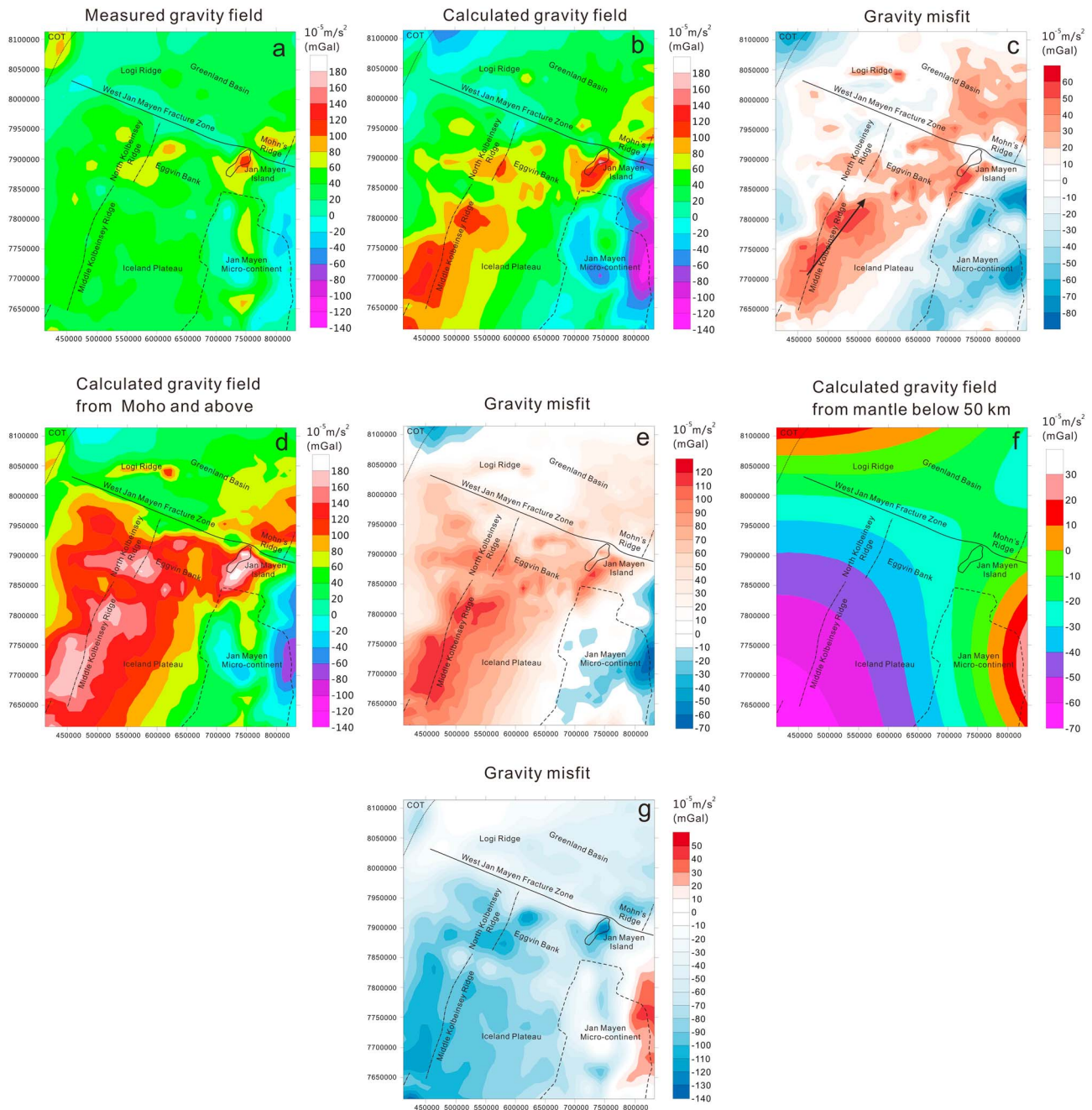
Figure 5. (a) Observed gravity field; free air gravity anomaly offshore and the Bouguer anomaly for the Jan Mayen Island (Gaina et al., 2011). (b) Gravity field calculated for the initial 3-D density model with homogeneous mantle density (3,300 kg/m³) between Moho and 50 km. (c) The gravity misfit is the calculated field subtracted the observed field. Blue colors indicate a mass deficit in the model, while the red areas show mass excess. The black arrow indicates the NE-SW axis of maximum positive gravity anomalies. (d, e) The calculated gravity response induced only by masses located above the Moho, and the gravity misfit made by subtracting the observed field from it. (f, g) The calculated gravity field from the mantle below 50 km, and the gravity misfit made by subtracting the observed field from it.

Figure 6a presents the resulting average mantle density for depths shallower than 50 km. This configuration shows lower densities of <3220 kg/m³ under the MKR and in an area close to Mohn's Ridge spreading axis, but significantly higher density (3,250–3,270 kg/m³) in the middle northern part of the study area (red line in Figure 6a). Then, we modified the initial 3-D density model by substituting the homogeneous density of the shallowest mantle by the inverted average densities (Figure 6a) and recalculated the gravity response of the entire model (using IGMAS+). This calculation results in the new gravity misfit field shown by Figure 6b.
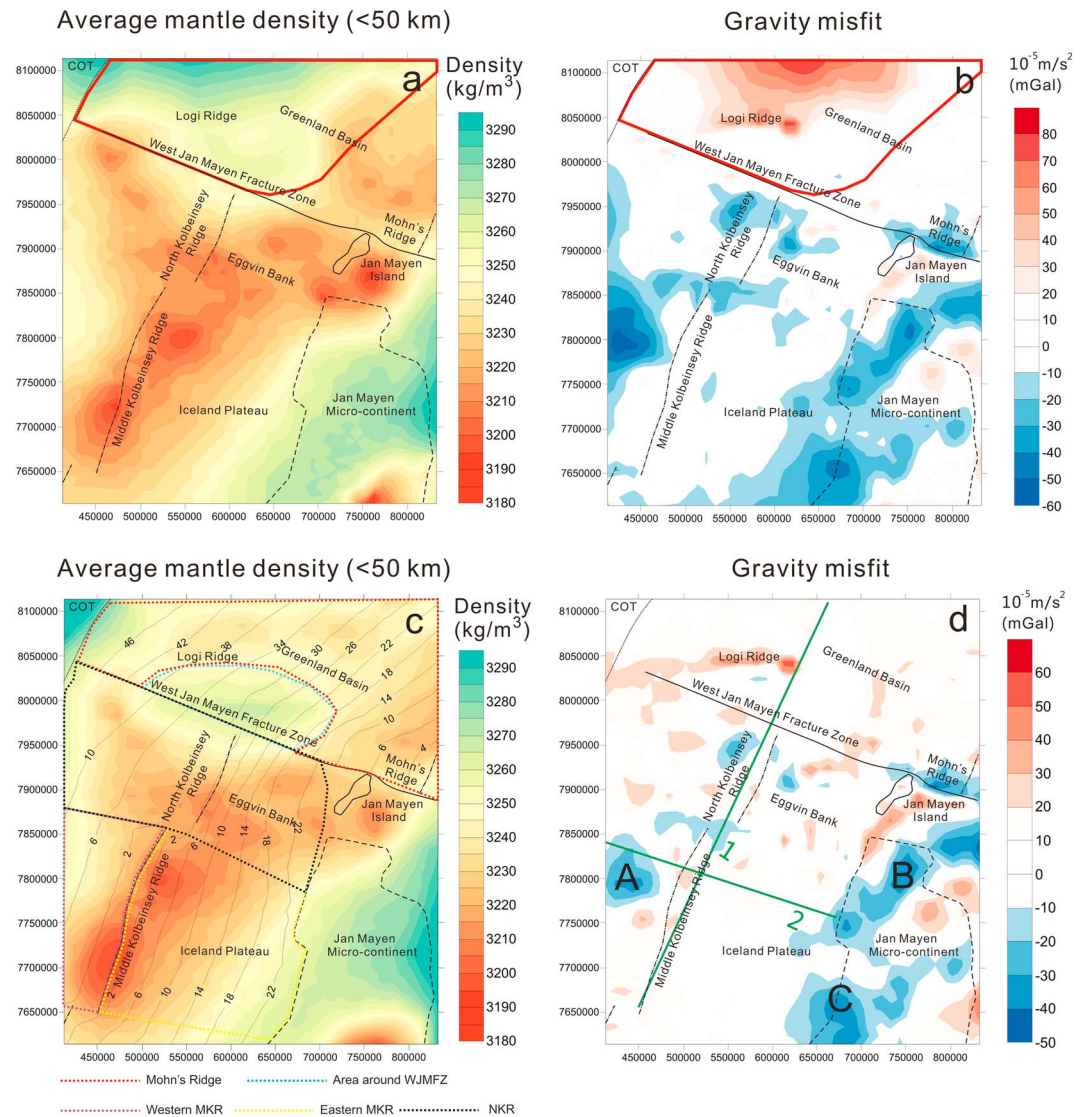
Figure 6. (a, b) Results of first gravity inversion run. Average mantle density between the Moho and 50-km depth (a), and gravity misfit (modeled gravity minus observed gravity, b). For this inversion run, the density configuration of the *seeds* layer has been set equal to the V_s derived densities at 50-km depth (Figure 4b). The red line delineates the area for which the estimated mantle temperature at 50-km depth is less than 900 °C (Figure 4a). (c, d) Results of second gravity inversion run. Average mantle density between Moho and 50-km depth (c) and gravity misfit (d). For the second inversion run, the maximum density of the seed layer has been set to 3,210 kg/m^3, which leads to a modification of the density model in the northern parts of the study area (red line in Figure 6a). The solid gray lines with numbers show the oceanic seafloor ages (Müller et al., 2008). Five different domains (Mohn's Ridge, area around WJMFZ, western MKR, eastern MKR, and NKR) are shown by color-coded dotted lines. Two green lines show positions of the sections of Figures 9 and 10. Points A–C represent the main anomaly misfits.

The gravity misfit map (Figure 6b; RMS: 20.37 mGal) shows that the middle northern parts of the study area are characterized by a large positive gravity misfit (up to 70 mGal), which indicates mass excess in this domain of the model. Because the density reduction of the upper 50 km of the mantle is restricted by the density of the seed, this prevents the uppermost mantle to obtain arbitrarily low densities, and thus, there can still be a gravity misfit after this first inversion step. This area of model mass excess is observed within the area of temperatures lower than 900 °C (outlined by the red line in Figure 6b), where the conversion to temperature and density has the largest uncertainties (Priestley & McKenzie, 2013). These uncertainties allow for changing the starting conditions for a second inversion run. In order to reduce the mass excess, the seed density was lowered from the 3,210- to 3,280-kg/m^3 range to a uniform 3,210 kg/m^3 for this region, corresponding to 900 °C at 50-km depth.

Table 3
Sensitivity Analysis of Various Parameters of the Sedimentary and Crustal Model on the Gravity Response and Induced Variation of the Uppermost Mantle Density

	Parameter	Imposed variations	Gravity response differences (mGal)			Uppermost mantle density variations (kg/m^3)		
			MKR	NKR	Mohn's	MKR	NKR	Mohn's
Z	Basement	Equal to bathymetry	2	2	10	<10	<10	<10
	Basement	+1.5 km	2	2	3	<10	<10	<10
	Top of lower oceanic crust	±1.5 km	∓20	∓20	∓20	<±10	<±10	<±10
	Top of lower oceanic crust[a]	±3 km		∓30			±20	
	Moho	±1.5 km	∓15	∓12	∓15	±10	±10	<±10
	Moho[a]	±3.0 km		∓20			±15	
ρ	Sediment	Assigned 2,650 kg/m^3	1	2	10	<10	<10	<10
	Upper oceanic crust	+20 kg/m^3	20	20	15	10	10	<10
	Upper oceanic crust	−10 kg/m^3	−10	−10	−8	<10	<10	<10
	Lower oceanic crust	±10 kg/m^3	±25	±35	±12	∓15	∓25	<∓10

Note. MKR = Middle Kolbeinsey Ridge; NKR = North Kolbeinsey Ridge.
[a]These parameters have been tested for two different values, respectively, to reflect the larger depth uncertainty in the less constrained western part of the NKR.

The average mantle density distribution from the second inversion run is shown in Figure 6c, and the corresponding misfit in Figure 6d. As reflected in the initial gravity misfit field (Figure 5c), the mantle density below the MKR is characterized by a NE-SW trending anomaly of low density (3,180–3,200 kg/m^3) with densities gradually increasing perpendicular to this virtual axis. Interestingly, the NE-SW elongated mantle anomaly does not, however, coincide entirely with the NNE-SSW striking ridge axis. The NKR domain is characterized by intermediate mantle densities (3,200–3,240 kg/m^3). In the region of the Greenland basin, close to the Mohn's Ridge spreading axis, the average mantle density is around 3,220 kg/m^3, slightly increasing to 3,240 kg/m^3 away from the spreading axis, with a sharp increase to 3,280 kg/m^3 at the continental-ocean transition. In addition, some relatively high mantle densities (3,250 kg/m^3) are observed around the WJMFZ.

The obtained gravity response of the density model shows a good fit with measured gravity, having a RMS deviation of 15.34 mGal (Figure 6d). In the oceanic crustal domains, the long-wavelength NE-SW gravity misfit (Figure 5c) as well as the large positive gravity misfit in the north (Figure 6b) have been removed, and the majority of the final gravity misfits range between ± 10 mGal (Figure 6d). However, some short-wavelength negative misfits (up to −30 mGal) are found in the northwestern parts of the MKR (Figure 6d, point A). In addition, the northern (Figure 6d, point B) and southwestern margins of the JMMC (Figure 6d, point C) have negative misfits up to −40 mGal.

3.6. Sensitivity Analysis

For the sedimentary and crustal layers, the resolution of the model is controlled by the coverage of constraints of the model layers. Areas where the initial sedimentary and crustal model derived its structure from interpolation and extrapolation across large distances have the greatest uncertainties. Thus, the most uncertain areas are the western part of the NKR domain, while the MKR domain and Mohn's Ridge are better constrained. Compared to previous 3-D gravity/seismic studies (Funck et al., 2016; Haase et al., 2016; Hermann, 2013), recently published seismic refraction and reflection results allowed for some improvements with regard to the distribution of sediment around the Logi Ridge (Breivik, Mjelde, Rai, & Frassetto, 2012) and the deep structure of the crystalline crust over the eastern part of the Eggvin Bank within the NKR domain (Tan et al., 2017).

We tested the sensitivity of the gravity response of the entire model with regard to both density and layer thickness variations. Our analyses focus on the differences between the three domains: MKR, NKR, and Mohn's Ridge (Figure 6c). Table 3 gives an overview of the models tested and respective parameters changed. Concerning the depth of the oceanic basement (which is relatively well constrained due to the small amounts of sediments and good seismic coverage), we have tested the effects of (i) setting it equal to the bathymetry and (ii) shifting it downward by 1.5 km. With the value chosen, we are testing an extreme scenario given that the uncertainty of this parameter typically is much smaller. For the top of the lower crust and the depth of the Moho, the Moho depth uncertainty of the western part of the NKR domain (not covered by seismic data) is given as ±3.0 km, while for the remaining parts it is ±1.5 km (Haase et al., 2016). We have assumed the

same uncertainty values for the top of the lower crust. Concerning the density of sediments, we have tested an unrealistic end-member scenario by assuming a largely compacted sediment sequence with a density of 2,650 kg/m^3. For the subsedimentary crustal units, we have tested extreme density values as derived from literature values (Table 2).

For each of the models tested, we have calculated the gravity response and the difference with respect to our preferred model. These *gravity response differences* are represented by their average values in Table 3. Although we have tested extreme values for the different parameters, the overall range of response differences obtained is significantly smaller compared to the gravity misfit distribution calculated for a homogeneous mantle at depths <50 km (Figure 5c). In addition, changing the input parameters would result in the inverted upper mantle densities to be changed by generally less than 10 kg/m^3. However, in the western NKR domain, the crust structure is less constrained and changes in lower crustal density and Moho depth might result in mantle density changes of up to 25 kg/m^3. Thus, there are some uncertainties for the density in the uppermost mantle beneath the western part of the NKR domain. This uncertainty will be further discussed in relation to interpretation of results in section 4.1.2.

In the MKR domain, the modeled uppermost mantle density anomaly increasingly deviates to the east of the spreading axis northward (Figure 6c). Checkerboard tests (Appendix A and Figure A1) show that the anomalously low density is reasonably well resolved down to the dimensions we observe. These tests suggest that the density anomalies may be underestimated as the dimensions become smaller, but there is no lateral displacement involved in the inversion process. In addition, the initial maximum gravity misfit (Figure 5c) runs slightly east from the spreading axis, indicating lower density there. A forward gravity modeling test shows that if we shift the low-density zone in the model back underneath the spreading axis, it will result in ~30-mGal gravity misfit. Thus, we believe that the anomalously low density in the uppermost mantle is not an artifact of the gravity inversion process.

Figure 5f shows that mantle density variations at depth of > 50 km mainly result in a long-wavelength gravity response, so that the change of the deeper mantle density would not remove the smaller-scale anomalies in the upper 50 km. Also, the initial gravity misfit (Figure 5c) does not spatially correlate with any of the subdomains (Figure 2d). Therefore, treating the subdomains differently in terms of composition or temperature-density relation would not improve the overall fit.

4. Discussion

4.1. Model Assessment
4.1.1. Density Configuration of the Sediments and Crust
Compared to the final density configuration of the shallowest mantle (Figure 6c), the gravity misfits are of shorter wavelengths (Figure 6d), which point to heterogeneities within the crust that are not resolved by the data constraints (Table 2). A short-wavelength gravity misfit low (up to −40 mGal) is observed in the northwestern part of the MKR (point A, Figure 6d). This is consistent with observed high-velocity lower crust (with densities of 3,050–3,100 kg/m^3) underlying this area (Hermann & Jokat, 2016; Weigel et al., 1995). However, since the spatial constraints of this high density layer are limited, it cannot be adequately traced, and is not incorporated into the model.

In addition, one negative short-wavelength gravity misfit (point B, Figure 6d) could potentially be explained by mafic intrusions into the JMMC, also not in the model (e.g., Blischke et al., 2016; Kandilarov et al., 2012; Kodaira et al., 1998a; Peron-Pinvidic et al., 2012a, 2012b). Another negative misfit is restricted to the southwestern boundary of the JMMC, where there are no seismic constraints (point C, Figure 6d). Prebreakup formation of the MKR is characterized by a long rifting period with significant conductive heat loss and accordingly not much magmatism generated (Kodaira et al., 1998b; Mjelde et al., 2008). The strong extension along the western boundary of the JMMC might have resulted in shallower Moho depths than used in the crustal model (Figure 2d), which if implemented would improve the gravity fit there.

4.1.2. Gravity Constrained Mantle Density Between Moho and 50 km Depth
There are some published 2-D gravity models in the area based on seismic crustal constraints, and a few also have additional velocity measurements of the uppermost mantle (Hermann & Jokat, 2016; Kandilarov et al., 2012, 2015; Peron-Pinvidic et al., 2012a, 2012b; Voss & Jokat, 2007; Weigel et al., 1995). However, none of these studies constrain the deeper velocity and hence the density of the mantle lithosphere and thus cannot be directly compared to our modeling results. The 3-D model by Haase et al. (2016) solved the density
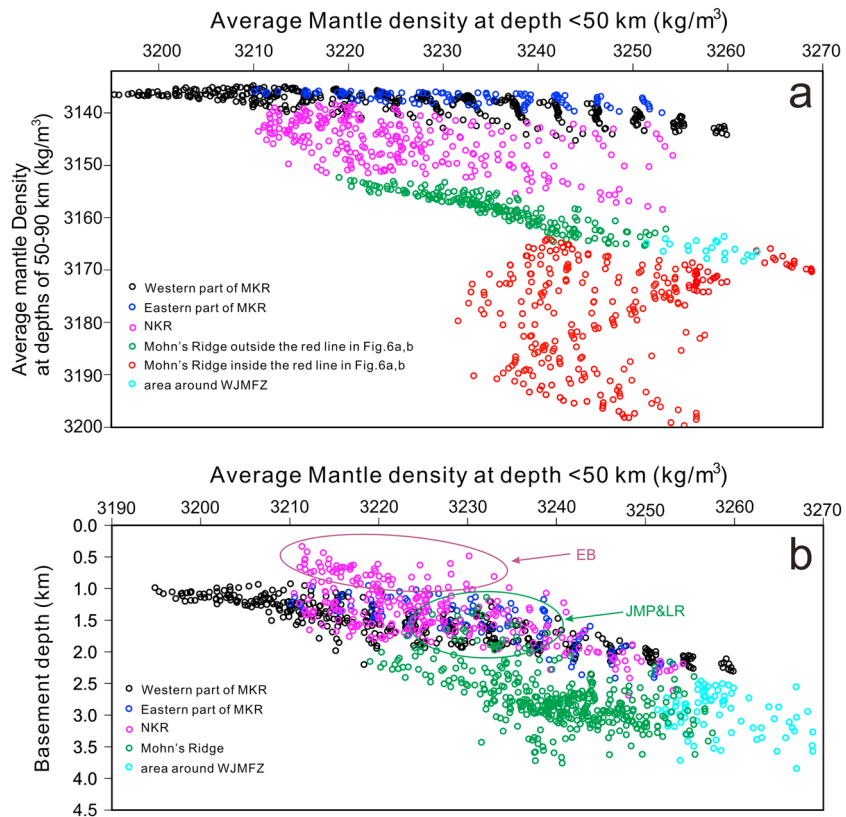
Figure 7. (a) Comparison of mantle density derived for different depths levels (<50 and 50-90 km, P_{50-90}, respectively) with colors showing different subdomains of the study area. Under the Mohn's Ridge, red dots represent ρ_{50-90} within the area of less than 900 °C at 50-km depth (red line in Figures 6a and 6b), while green dots indicate the ρ_{50-90} outside this subdomain. (b) Comparison of gravity-constrained mantle density (<50 km) and basement depth (corrected for sediments loading). Arrows indicate local geological features departing from the expected trends: Eggvin Bank (EB), Jan Mayen Plateau (JMP), and Logi Ridge (LR; Figure 1). WJMFZ = West Jan Mayen Fracture Zone; MKR = Middle Kolbeinsey Ridge; NKR = North Kolbeinsey Ridge.

structure of the lithosphere by forward temperature models based on lithspheric age and miss some of the plume-induced temperature variations that are clearly present.

In this study, the mantle density at depths <50 km is a result of gravity inversion, while mantle density at depths >50 km is derived from *S* wave velocities. Despite the different types of constraints on density, there should be a positive correlation between the two. We have plotted average mantle density between 50 and 90 km (ρ_{50-90}) against the gravity-constrained density of the shallowest mantle for the entire oceanic domain (Figure 7a). The MKR domain has significantly lower ρ_{50-90} compared to the Mohn's Ridge, indicating the Iceland plume influence there. Despite the independence of constraints (*S* wave velocity, respectively gravity) and the artificial, methodologically imposed separation of the two mantle domains, there is a strong correlation between the two for the areas near the Mohn's Ridge (green points; Figure 7a), where the correlation coefficient (*R*) is 0.84. MKR and NKR domains have a weaker correlation with a correlation coefficient of 0.69 and 0.54, respectively. However, for the northwestern Mohn's Ridge subregion (red points) where derived mantle temperatures at 50 km depth are <900 °C and the accuracy of the V_s-to-*T* conversion is reduced (Priestley & McKenzie, 2006, 2013), there is a poor correlation (*R* = 0.20). Accordingly, the gravity-inverted densities are associated with larger uncertainties in this region.

In terms of density and temperature, the NKR takes an intermediate position between the MKR and the Mohn's Ridge, but the linear correlation between the shallow and deep mantle densities is much less pronounced. Therefore, factors other than temperature might control density variations in the NKR. A recent seismic study shows that the anomalously shallow NKR domain relates to thick crust (Tan et al., 2017). Apart from this study, the crustal model in the western part of the NKR domain is not well constrained, as it is derived from previous gravity inversion (Haase et al., 2016). Therefore, both the less constrained crustal model and a heterogeneous

mantle source under the NKR domain (e.g., Haase et al., 2003) could contribute to a weaker correlation (R = 0.54) between ρ_{50-90} and average mantle density at depths <50 km.

Basement depth and topography/bathymetry are isostatically controlled by variations in the crustal thickness, upper mantle densities, and sediment load (Stein & Stein, 1992). To calculate basement depth corrected for sediment loading (B_s), a standard Airy isostatic correction (Le Douaran & Parsons, 1982) was applied:

$$B_s = B + (\frac{\rho_w - \overline{\rho_s}}{\rho_a - \rho_w})Z_s \qquad (7)$$

where B is the depth to the top basement (Figure 2a), ρ_a is the density of asthenospheric mantle (3,200 kg/m^3), ρ_w is the density of water (1,030 kg/m^3), and Z_s is the thickness of the sediment units (Figure 2b). The average density of the sedimentary column ($\overline{\rho_s}$) is calculated based on our crustal density model (Table 2).

Except for some oceanic islands and plateaus (e.g., Eggvin Bank and Logi Ridge), crustal thickness is relatively uniform within each of the three different domains (MKR: 8–9.5 km, NKR: 10–11 km, and Mohn's Ridge: 3–5 km; Figure 2). Thus, we can discuss basement depths as being mostly controlled by mantle density variations within each domain. We have plotted corrected basement depth against gravity-constrained average mantle density at depths <50 km (Figure 7b). Not surprisingly, the oceanic domain overall shows a positive correlation indicating that the study area is locally in isostatic equilibrium. Some deviations from the main trends (marked in the Figure 7b) indicate local geological features with shallower bathymetry and thicker crust.

Basement depth of the oceanic plate corrected for sediment loading has a linear relation with the square root of the seafloor age (Myr$^{1/2}$) if subsidence is controlled by passive thermal cooling only (e.g., Adam & Vidal, 2010; Stein & Stein, 1992). Linear regression shows a trend at the Mohn's Ridge of 300 m/Myr$^{1/2}$ (Figure 8a), which is comparable to normal seafloor subsidence rate at 320 m/Myr$^{1/2}$ (Korenaga, 2008). However, the eastern MKR younger than 10 Ma shows a subsidence rate of about 230 m/Myr$^{1/2}$, while the subsidence rate for oceanic ages older than 10 Ma increases to around 390 m/Myr$^{1/2}$. The youngest western MKR has a subsidence rate of about 200 m/Myr$^{1/2}$ but increases to 490 m/Myr$^{1/2}$ for oceanic ages older than 4 Ma (Figure 8a). Thus, the observed trends show a substantial deviation in mantle thermal structure compared to the theoretical half-space cooling model. The poor correlation between the basement depth and oceanic ages observed under the NKR domain is on the other hand, most likely related to large crustal thickness variations as mapped in the eastern NKR by Tan et al. (2017).

Similarly, the average mantle density at depths < 50 km derived from the half-space cooling model shows a positive trend with the square root of the seafloor age (Myr$^{1/2}$; Figure 8b; Sandwell, 2001). However, under the MKR domain the density distribution of the upper mantle (<50 km) differs somewhat from that and is asymmetric with lower density east of the spreading axis (Figures 8b and 10). Consistent with the thermal subsidence deviation, the mantle density at eastern MKR domain for seafloor ages less than 10 Ma is slightly lower than expected from the half-space cooling model (yellow line in Figure 8b). The yellow line shows the age-dependent average mantle density (<50 km) based on lithospheric thermal structure from Sandwell (2001) and conversion of these temperatures to density following the method in section 3.3.2. A sharp increase in mantle density is observed for seafloor ages older than 10 Ma (Figure 8b). On the other hand, the density distribution of the Mohn's Ridge at age between 6 and 25 Ma follows the half-space cooling model but shows slightly less density older than 25 Ma and higher for younger than 6 Ma. This is consistent with little impact from the Iceland plume near the spreading zone. The mantle density under the NKR domain has large variations and there is no correlation between the density and oceanic age (Figure 8b). The lack of correlation is most likely related to a complex development where off-axis magmatic intrusions affect seafloor depth and crustal thickness (Tan et al., 2017). Uncertainty in the crustal thickness in the western NKR also make upper mantle densities less well constrained, and could contribute to this.

In order to address this uncertainty, we show a map of basement depth corrected for sediment loading and age-controlled subsidence (assuming subsidence rate at 320 m/Myr$^{1/2}$ and depth of the spreading axis at 2,600 m; Stein & Stein, 1992; Figure 8c). The result shows that the residual basement of Mohn's Ridge has almost no variations, while in the northern parts of the MKR, the residual basement of the eastern part of the spreading ridge is about 300 m shallower than the remaining MKR domain, consistent with Figure 8b. Similarly, the eastern NKR is 600 m shallower than western part. The regions of shallow depths (< 2000 m) do largely correlate with regions of low calculated average mantle density < 3,250 kg/m^3 at depths less than 50 km (Figure 6c).
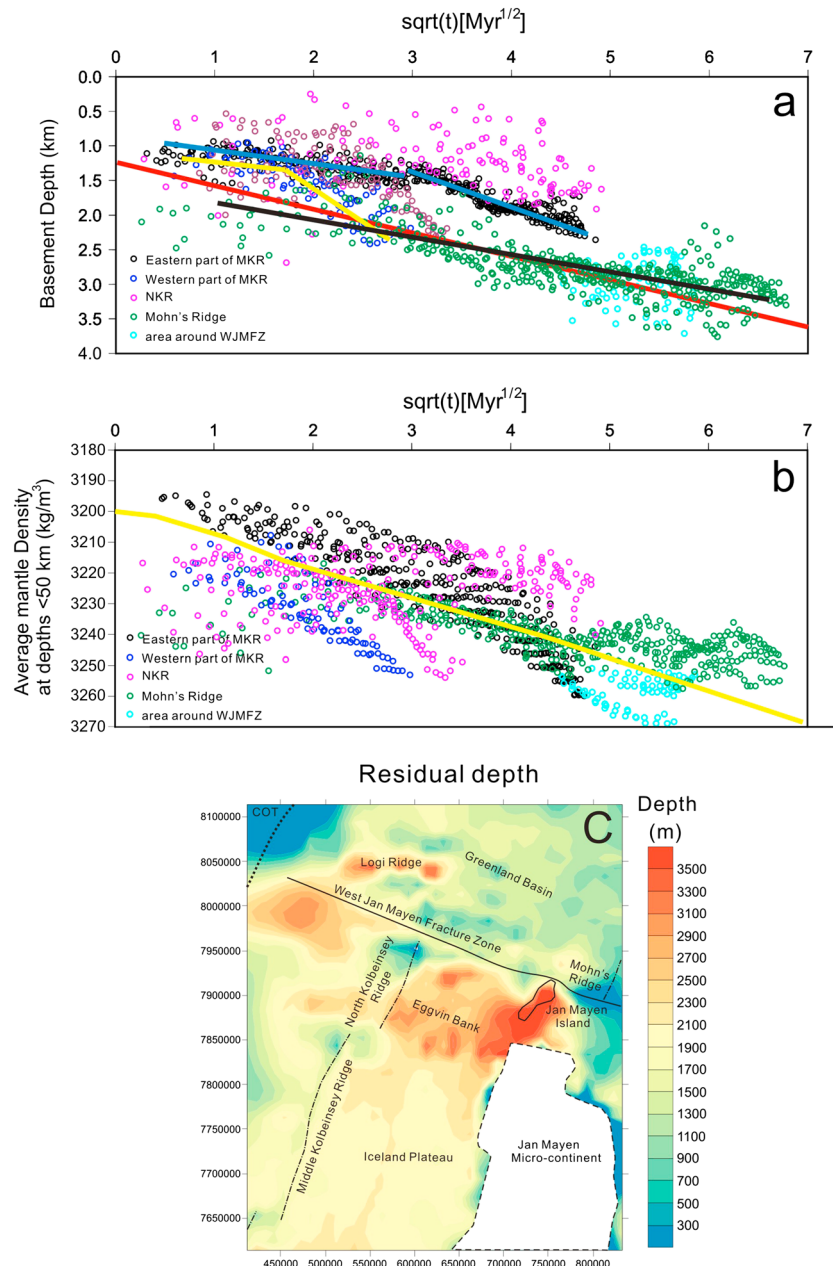
Figure 8. (a) Observed basement depth (corrected for sediment load) against the square root of seafloor age (Müller et al., 2008) for different subdomains of the study area. Red solid line: a normal seafloor subsidence rate of 320 m/Myr$^{1/2}$ (Korenaga, 2008), blue line: eastern MKR, yellow line: western MKR, and black line: Mohn's Ridge. (b) Mantle density at depths <50 km against the square root of seafloor age for different subdomains of the study area. The yellow line illustrates the age-dependent average mantle density (<50 km) based on Sandwell (2001). (c) Residual basement depth is corrected for sediment loading and subsidence with seafloor age using a seafloor subsidence rate at 320 m/Myr$^{1/2}$ and a spreading axis depth at 2,600 m (Stein & Stein, 1992). WJMFZ = West Jan Mayen Fracture Zone; MKR = Middle Kolbeinsey Ridge; NKR = North Kolbeinsey Ridge; COT = Continent Ocean Transition Zone.

An anomalously deeper residual basement of the western NKR allows for a colder mantle or a thinner crust. Isostatic analysis shows that 600 m deeper basement can be balanced by an increase of uppermost mantle density by 25 kg/m^3. This is consisted with our gravity-derived uppermost mantle density, where the difference between the average uppermost mantle density between the eastern (3,220 kg/m^3) and western NKR (3,240 kg/m^3) is 20 kg/m^3. Alternatively, the deeper residual basement could be caused by crustal thickness variations, where a 600 m deeper basement of the western NKR can be balanced by a decrease of Moho depth

of about 1 km. However, a decrease of Moho depth of 1 km gives a decrease of uppermost mantle density < 10 kg/m^3 (Table 3). In this case, the eastern NKR still needs less dense mantle compared to western part. A sensitivity test shows that if the Moho depth of western NKR domain is decreased by 3 km, then this would make the uppermost mantle density more symmetrical over the NKR. However, with a symmetrical low-density distribution, the present magmatism along the NKR would show melting under elevated mantle temperature, but this is inconsistent with geochemical studies (e.g., Elkins et al., 2016; Haase et al., 2003). Also, the eastern displacement of the negative uppermost mantle density anomaly under the NKR is continuous with that of the better constrained MKR domain to the south, as well as to that of the southern Mohn's Ridge to the north, suggesting that our preferred model is reasonable. Nevertheless, additional seismic surveys around the NKR would be needed to better constrain the development of this area, and to determine to what extent the influence of the Iceland plume has varied over time at the northern tip of the Kolbeinsey Ridge.

4.1.3. Density Configuration of the Deeper Mantle (>50 km)

The mantle temperature estimated from V_s has uncertainties, since the empirical relationship was derived from observations in the Pacific Ocean (Priestley & McKenzie, 2006). However, this relationship is comparable to that of a recent study of Schoonman et al. (2017), who postulate an empirical relationship between observed surface residual elevation, temperature, and shear wave velocity for the mantle of northern Britain and western Norway. In addition, the V_s-derived temperature configuration (T_{50-90}; Figure 4c) is indirectly validated by the observed crustal thickness (Figure 2d). Accordingly, the crustal thickness difference between the present-day spreading axis of the MKR and Mohn's Ridge (4–4.5 km; Figure 2d) indicates that the mantle potential temperature under the MKR is elevated by about 75 °C (Ito & Lin, 1995). This is consistent with the difference in the T_{50-90} around the present-day spreading axis of MKR (1350°C) and Mohn's Ridge (1270 °C), which is 80 °C (Figure 4c).

Our Vs-temperature-density calculations are based on the assumption that the mantle composition is homogeneous. There appears to be a homogeneous, depleted mantle source under the MKR (e.g., Elkins et al., 2011) and Mohn's Ridge (e.g., Klingelhöfer, Géli, & White, 2000) but a heterogeneous enriched mantle under the NKR (e.g., Haase et al., 2003). A variation of the mantle composition below the melt zone could affect V_s, producing discrepancies in derived mantle temperature, and accordingly mantle density estimates (Goes & Van der Lee, 2002). Several studies (Priestley & McKenzie, 2006, 2013; Schutt & Lesher, 2006), however, suggest that the mantle composition variations are difficult to resolve from seismic tomography. Moreover, the velocity anomalies caused by compositional changes are unlikely to exceed 1% (Priestley & McKenzie, 2006; Schutt & Lesher, 2006). A change in V_s of 0.04 km/s would result in a 40 °C and 6-kg/m^3 difference at a temperature of 1300 °C (Figure 3). Sensitivity tests performed for the 3D density model presented here shows that a decrease of the mantle density at depth between 50 and 90 km by 1% under the MKR domain results in a gravity response with average 14-mGal difference. This indicates that the derived density heterogeneities at greater mantle depths (>50 km) exert minor control on the gravity field compared to shallower mantle and crustal structure.

The upper oceanic mantle density is also affected by melt extraction from the mantle beneath spreading ridges, causing chemical depletion of the residual solid (e.g., Jha et al., 1994; Oxburgh & Parmentier, 1977; Schutt & Lesher, 2006; Scott & Stevenson, 1989). However, the part of the mantle that has undergone the highest melt degree by ascent through the whole melt zone is located in the shallowest part and will mostly fall within the region where we invert for density, and the effect should therefore be incorporated in the modeling results.

Another uncertainty is the potential presence of a melt fraction within the mantle. Priestley and McKenzie (2006) argue that the fraction is generally small (< 0.1%) and has little effect on the V_s to temperature conversion. While some authors argue that the low seismic velocities observed in the upper asthenosphere can be adequately explained without much melt (e.g., Stixrude & Lithgow-Bertelloni, 2005), other observations indicate that some unmobilized melt up to a few percent could be present locally (Naif et al., 2013; Rychert & Shearer, 2009). The V_s model has low resolution, was sampled at a 100-km grid, and will not delineate the spreading ridges well. However, we note that the V_s distribution is reasonably well centered on the spreading ridges (Figures 4a and 4c), which may be a combined effect of melt and elevated temperature. However, it is not obvious that a small melt fraction should affect the V_s significantly. The formation of melt would extract water from the mantle, which will increase the velocity of the solid. With fractional melting, the net effect could be a slight velocity increase in total (e.g., Karato & Jung, 1998). That the modeled low-density anomaly shows an increasing discrepancy from the spreading ridge position to the north and correlates well
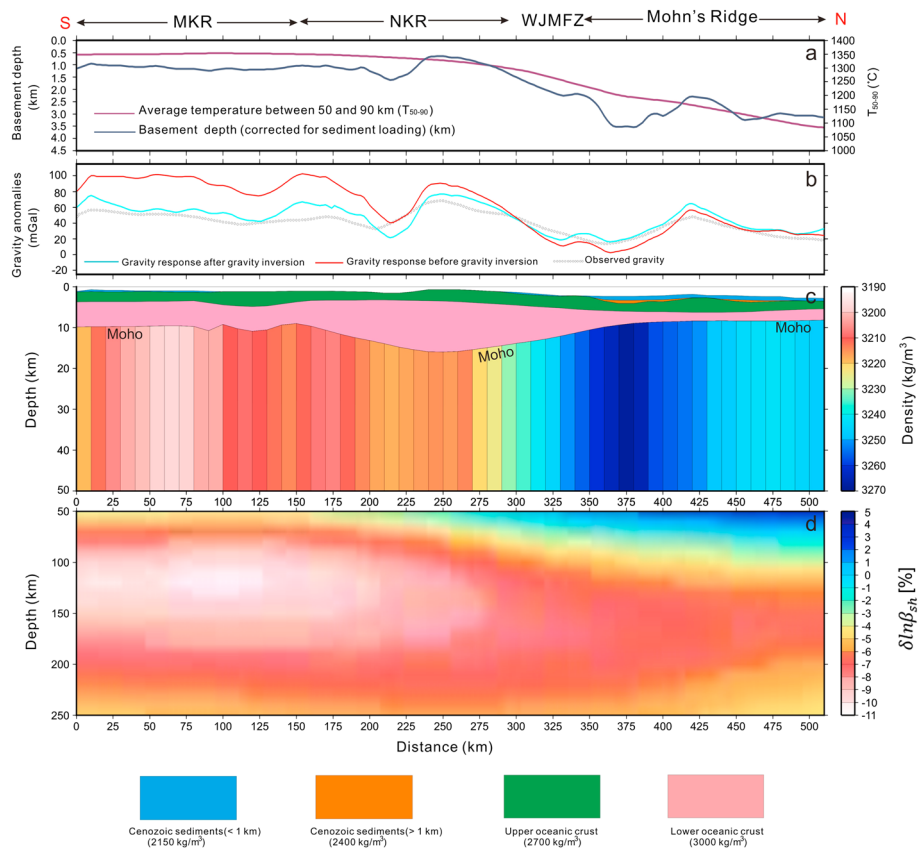
Figure 9. Results of the 3-D gravity modeling along a N-S directed section through the study area (green line 1 in Figure 6d). (a) Basement depth and average mantle temperature (T_{50-90}) between 50- and 90-km depth (Figure 4c). (b) The corresponding observed and calculated gravity before and after gravity inversion. (c) Vertical section through the 3-D model with vertical average mantle density configuration between the Moho and 50-km depth (Figure 4d). (d) S wave relative velocity perturbations ($\delta \ln \beta_{sh}$, %) in the deeper mantle from Rickers et al. (2013). MKR: Middle Kolbeinsey Ridge, NKR: North Kolbeinsey Ridge, and WJMFZ: Western Jan Mayen Fracture Zone.

with anomalously low seafloor subsidence (Figure 8) suggests that it is not an artifact of the V_s to temperature conversion assumptions. The V_s-derived mantle density gives a long-wavelength density distribution (Figure 5f) that cannot be predicted from the age of the oceanic lithosphere alone and should improve the inversion results considerably. Absolute densities may be affected near the spreading ridges if retained melt changes the V_s-temperature relationship, but the trend of the uppermost mantle low-density anomaly that we find should be robust.

4.2. Plume-Lithosphere Interaction

The WJMFZ represents a main mantle temperature contrast (Figure 4c). North of the WJMFZ, the Greenland Basin is characterized by thinner crust, larger basement depth, higher mantle density, and lower mantle temperature compared to the NKR domain (Figure 9). This is illustrated by calculating lithospheric thickness from the age grid of Müller et al. (2008) using the approach of Zhang and Lay (1999) (Figure 11). There is a significant thickness increase from the NKR to the Greenland Basin to the north. Approximately midway between the northern tip of the Kolbeisney Ridge and Jan Mayen, the lithospheric thickness is predicted to be similar on both sides of the WJMFZ. Farther to the east, the lithoshere should be thinnest north of the WJMFZ, close to the Mohn's Ridge. Such steps in the lithosphere-asthenosphere boundary have been postulated to control the emplacement of plume material (*plume ponding*; Sleep, 1997) and could potentially accumulate plume material from a northward flow out from the Iceland plume under the Eggvin Bank, if the flow was strongly directed by the spreading ridge.

Elkins et al. (2016) and Schilling (1999) argue that excess magmatism in the NKR domain is caused by a putative Jan Mayen plume. However, Mertz et al. (2004) argue that the plume does not follow a simple time-transgressive track and cannot explain the radiogenic Nd-Pb isotope compositions of basalts from the
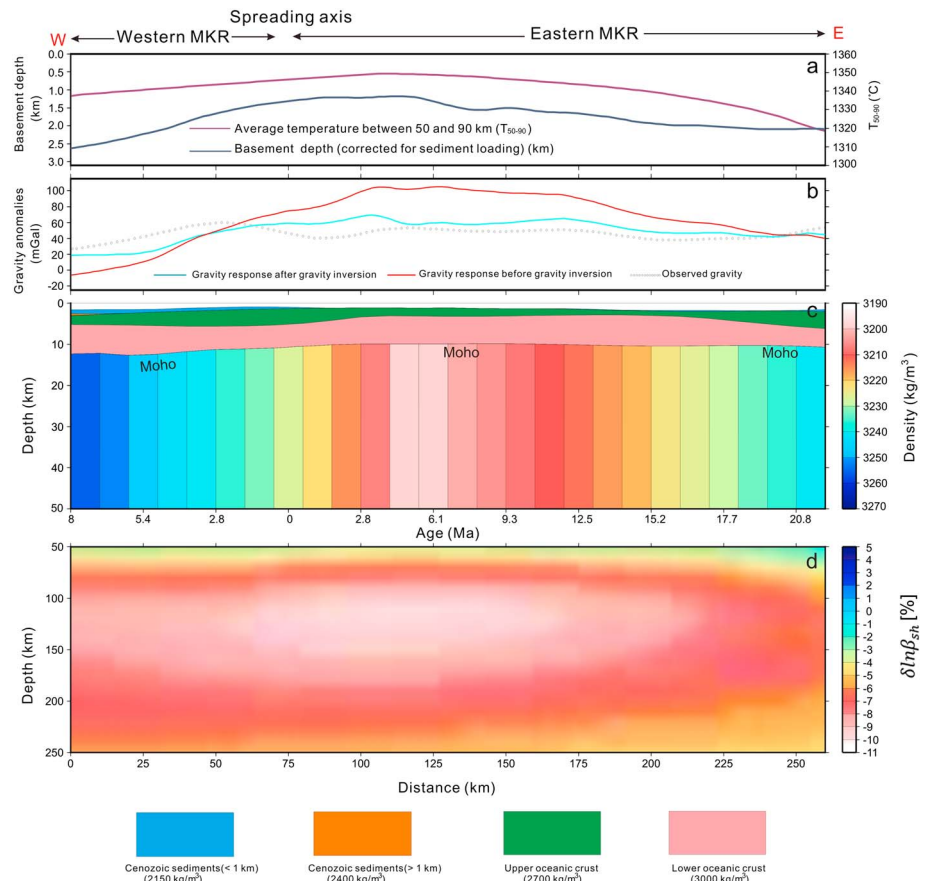
Figure 10. Results of the 3-D gravity modeling along a W-E directed section through the study area (green line 2 in Figure 6d). (a) Basement depth and average mantle temperature (T_{50-90}) between 50- and 90-km depth (Figure 4c). (b) The corresponding observed and calculated gravity before and after gravity inversion. (c) Vertical section through the 3-D model with vertical average mantle density configuration between the Moho and 50-km depth (Figure 4d). (d) S wave relative velocity perturbations ($\delta ln\beta_{sh}$, %) in the deeper mantle from Rickers et al. (2013). MKR: Middle Kolbeinsey Ridge.

NKR. The Eggvin Bank excess magmatism appears not to be governed by elevated temperature (Haase et al., 2003), but by an enriched mantle component, probably over some time (Tan et al., 2017), and at least does not require a thermal mantle plume. Jones et al. (2002) document V-shaped ridges along the Kolbeinsey Ridge up to the end of the MKR segment, taken to indicate transport of mantle zones with variable temperature from the Iceland plume. It shows an apparent propagation speed that is still quite high in the northernmost part (100–150 mm/Ma) and a counter flow from a potential Jan Mayen plume is therefore not expected there.

South of the WJMFZ, a tomography model shows a strong low-velocity anomaly located in the upper mantle (90–150 km) beneath the MKR domain (Figures 9 and 10). Velocity perturbations here reach between −9% and −11%, indicating high-temperature and reduced asthenospheric density there. The shallower mantle depth between 50 and 90 km resembles this, where our density model shows a high temperature (T_{50-90} > 1340 °C; Figure 4c) and a low-density (ρ_{50-90} < 3140 kg/m^3; Figure 4d) anomaly at a broad region. However, the shallow mantle density anomaly at depths of < 50 km is much narrower (Figure 6c). In the south, the uppermost mantle density anomaly lies underneath the spreading ridge and should reflect the cooling of the lithosphere as it moves away from the ridge. Judging from the 9- to 11-km oceanic crustal thickness south of our study area, it is also affected by hot plume material in the axial zone (Hooft et al., 2006). However, the center of the low-density anomaly increasingly deviates to the east of the spreading ridge northward. We interpret this deviation to be the effect of lithospheric heating from plume flow in the upper asthenosphere below (not resolved by the tomography model). In this sense, it represents thermal erosion of the lithosphere that will make the temperature structure and thickness deviate from what is expected from a passive cooling model based on age, as shown in Figure 8. The obtained density model for the mantle shallower than 50 km
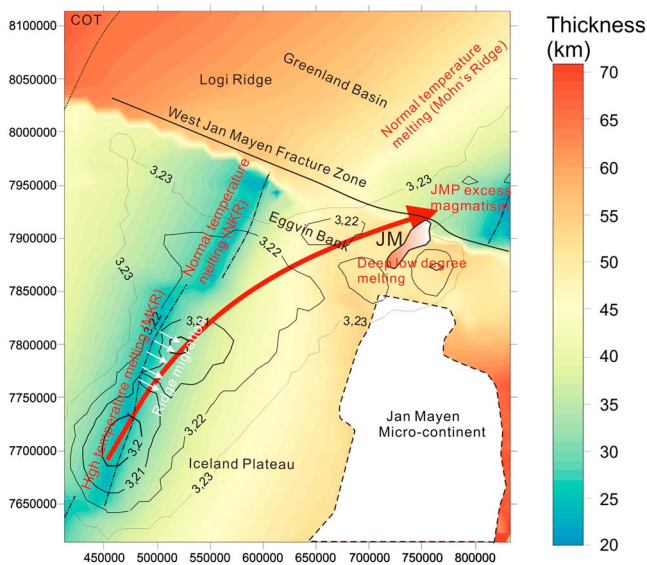
Figure 11. Estimated oceanic lithosphere thickness for the study area based on the crustal age model of Müller et al. (2008) using the approach of Zhang and Lay (1999). The solid black lines with numbers show contours of the uppermost mantle densities less than 3.23 g/cm³, where thicker lines correspond to lower densities (Figure 6c). JM: Jan Mayen; JMP: Jan Mayen Plateau.

will mostly encompass the lithosphere and show this thermal influence. The lowest mantle densities from the model are contoured on top of the age-based lithospheric thickness grid in Figure 11. The zone of lowest density passes under Jan Mayen toward the southern tip of the Mohn's Ridge. Thus, judging from the distribution of the lowest upper mantle density, the asthenospheric flow below appears to avoid the lithospheric thickness increase north of the Kolbeinsey Ridge and is instead redirected farther east toward the region where there is no obstacle in lithospheric thickness, as indicated by the red arrow in Figure 11. The eastward deviation of the uppermost asthenospheric flow may have existed for some time, as it correlates with other geological observations. In the south, the MKR axis underwent eastward ridge migration since approximately 5.5 Ma (Appelgate, 1997), following this deviation. Thus, the thermal erosion of the lithosphere on the east side of the MKR could be the driving force behind the eastward axial relocations (Figure 11). This redirection of the plume flow could also help to explain why the present spreading at the NKR does not appear to be influenced by elevated mantle temperature. Rather, it is known to be sourced from an enriched mantle component different from the MKR (e.g., Elkins et al., 2011, 2016; Haase et al., 2003). Thus, neither geochemical data nor our results can confirm a model where ponding of northward plume flow occurs against a lithospheric thickness increase at the northern end of the Kolbeinsey Ridge. While the upper asthenospheric plume flow appears to be influenced by spreading ridge location to some degree, it responds on a slightly larger, more regional scale, where it is determined by the change of lithospheric thickness north of the WJMFZ. Finally, we note that the flow passes underneath the presently volcanically active Jan Mayen Island, probably supplying the extra heat for a small degree of deep mantle melting to occur (Trønnes et al., 1999; Figure 11). Also, the oceanic crust around the southern tip of the Mohn's Ridge across the WJMFZ is thicker than normal, adjacent to the island on the same trend (Kandilarov et al., 2012; Figures 1 and 11).

5. Summary and Conclusions

A three-dimensional structural and density model of the crust and upper mantle is developed for the greater Jan Mayen-East Greenland region, in order to determine the influence of the Iceland mantle plume on the area. We obtain the 3-D density structure of the sedimentary cover and the crust down to the Moho mainly from regional reflection and refraction seismic lines. The deeper mantle temperature and density structure (>50 km) is derived from an S wave mantle tomography model (Rickers et al., 2013), while the shallower mantle density (<50 km) is determined by 3D gravity inversion. The V_s-derived mantle temperature and density show large variations at depths between 50 and 90 km. Based on present-day spreading axis segmentation, we divided the study area into MKR, NKR, and Mohn's Ridge regions (Figure 2d). In general, the model shows trends of decreasing average mantle temperature (T_{50-90}) and increasing density (ρ_{50-90}) between 50 and 90 km from MKR to NKR and to the Mohn's Ridge in the direction away from the plume.

Compared to the MKR domain, the greater basement depth, denser shallowest mantle, and cooler mantle temperature (T_{50-90}) under the Mohn's Ridge show much reduced plume influence here. The NKR, including the shallow Eggvin Bank, is bounded by two ridge offsets, where the WJMFZ has a long offset of 200 km, and represent a major lithospheric thickness contrast. Beneath the Kolbeinsey region, the uppermost mantle density shows a NE-SW elongated density anomaly. In the south, it coincides well with the spreading ridge but rotates clockwise away from the northern MKR and the NKR, toward the Mohn's Ridge when approaching the WJMFZ. This anomaly is interpreted to be the result of the Iceland plume flow to a large degree interacting with the base lithosphere topography on a regional scale. To some extent, the flow follows the spreading axis, but the large offset of the WJMFZ appears to form an obstacle since the lithospheric thickness increases to the north of the tip of the Kolbeinsey Ridge. Instead, the flow is deviated eastward toward the Mohn's Ridge, where the lithospheric thickness is similar or less to the north of the WJMFZ. This results in a marked east-west asymmetry across the northern MKR, where the western domain has higher mantle densities (<50 km) and a deeper top basement, which indicates lower lithospheric mantle temperature there. Under the eastern MKR
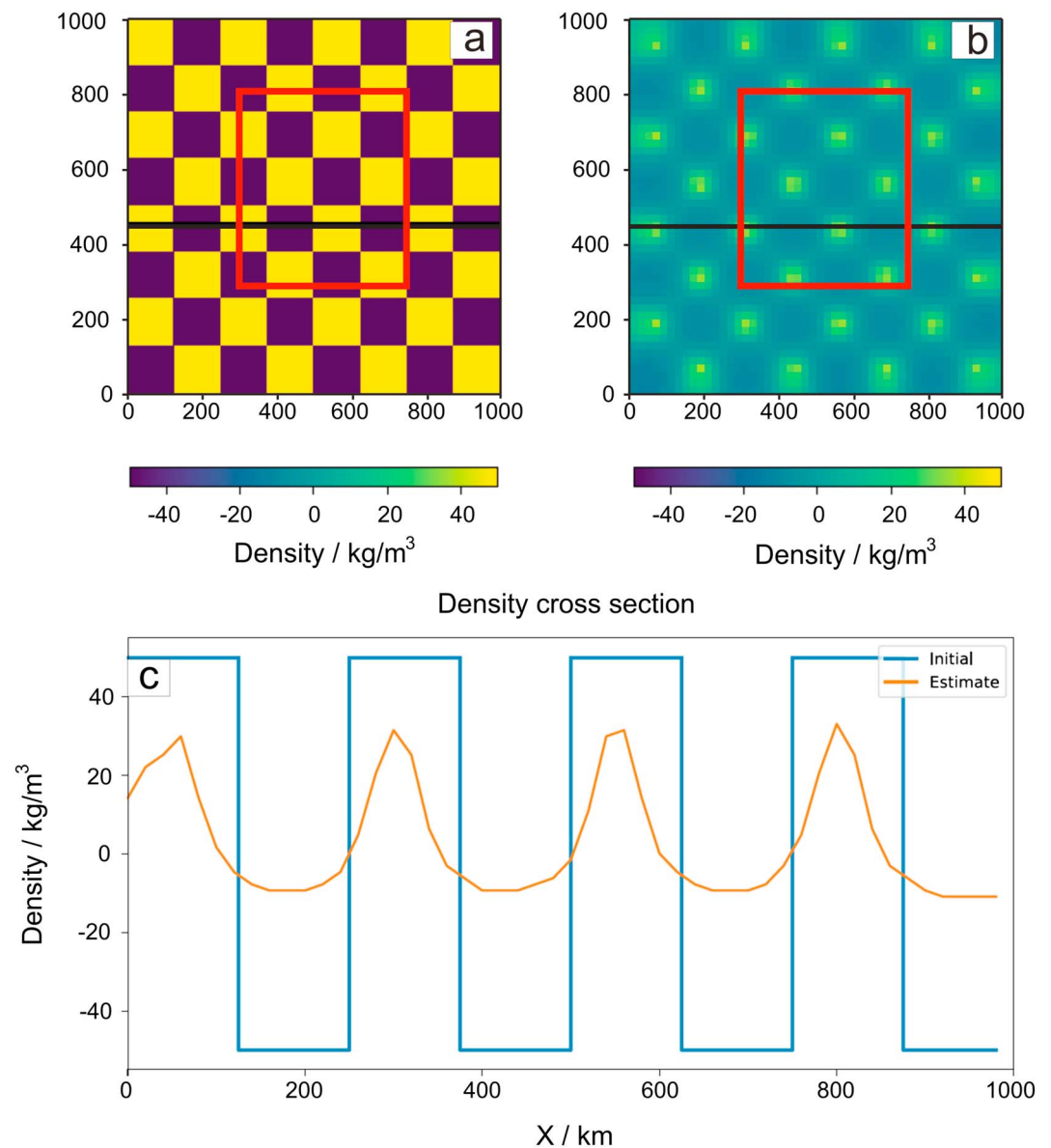
Figure A1. Checkerboard resolution test result performed using the gravity inversion algorithm *fatiando a terra* (Uieda et al., 2013). (a) Input density perturbations of ±50 kg/m³ with cell of 125 km × 125 km. (b) Recovered density perturbations from the checkerboard tests. (c) Input density and recovered density perturbations along a section (black line) in Figures A1a and A1b. Red boxes represent the size of our study area in relation to the extended model.

domain, the low mantle density anomaly lies east of the present day ridge axis. This results in a significant departure from the half-space cooling model, and the plume flow-induced thermal erosion on the east side of the ridge may be the cause for several eastward ridge relocations in the past 5.5 Ma (Appelgate, 1997). Also, the plume flow appears to deviate eastward of the NKR, consistent with the present lack of elevated mantle temperature in the melt zone underneath the ridge (e.g., Haase et al., 2003). Furthermore, it passes under the volcanically active Jan Mayen Island, across the WJMFZ and toward the thick oceanic crust surrounding the southern tip of the Mohn's Ridge, and it is the likely cause for both.

Appendix A: Checkerboard Test

To determine the resolution of the 3-D gravity inverse model, we imposed a checkerboard pattern with a dimension of 125 km × 125 km, and a density perturbation of ±50 kg/m³ in the uppermost mantle (Figure A1). This configuration is comparable to the regional anomalies we are investigating. The results show that the

inversion has an even response over the model area, without lateral offsetting the anomalies. However, the ability to recover the true amplitude of density anomalies seems significantly reduced at this scale, but the lateral dimensions of the anomalies are clearly resolvable. In reality, we do not expect strong density contrasts anywhere near what was used in the checkerboard tests, and the modeled density anomalies are expected to be nearer to the true values than seen in these tests.

References

Adam, C., & Vidal, V. (2010). Mantle flow drives the subsidence of oceanic plates. *Science*, *328*(5974), 83–85.

Appelgate, B. (1997). Modes of axial reorganization on a slow-spreading ridge: The structural evolution of Kolbeinsey Ridge since 10 Ma. *Geology*, *25*, 431–434.

Bai, Y., Williams, S. E., Müller, R. D., Liu, Z., & Hosseinpour, M. (2014). Mapping crustal thickness using marine gravity data: Methods and uncertainties. *Geophysics*, *79*(2), G27–G36.

Barton, P. J. (1986). The relationship between seismic velocity and density in the continental crust—A useful constraint? *Geophysical Journal of the Royal Astronomical Society*, *87*, 195–208.

Blischke, A., Gaina, C., Hopper, J. R., Péron-Pinvidic, G., Brandsdóttir, B., Guarnieri, P., et al. (2016). The Jan Mayen microcontinent: An update of its architecture, structural development and role during the transition from the Ægir Ridge to the mid-oceanic Kolbeinsey Ridge. *Geological Society, London, Special Publications*, *447*, 299–337. https://doi.org/10.1144/SP447.5

Brandsdóttir, B., Hooft, E. E. E., Mjelde, R., & Murai, Y. (2015). Origin and evolution of the Kolbeinsey Ridge and Iceland Plateau, N-Atlantic. *Geochemistry, Geophysics, Geosystems*, *16*, 612–634.

Breivik, A. J., Faleide, J. I., & Mjelde, R. (2008). Neogene magmatism northeast of the Aegir and Kolbeinsey Ridges, NE Atlantic: Spreading ridge–mantle plume interaction? *Geochemistry, Geophysics, Geosystems*, *9*, Q02004. https://doi.org/10.1029/2007GC001750

Breivik, A. J., Faleide, J. I., Mjelde, R., & Flueh, R. (2009). Magma productivity and early seafloor spreading rate correlation on the northern Vøring Margin, Norway—Constraints on mantle melting. *Tectonophysics*, *468*, 206–223. https://doi.org/10.1016/j.tecto.2008.09.020

Breivik, A., Mjelde, R., Faleide, J. I., Flueh, E., & Murai, Y. (2014). Magmatic development of the outer Vøring Margin from seismic data. *Journal of Geophysical Research: Solid Earth*, *119*, 6733–6755. https://doi.org/10.1002/2014JB011040

Breivik, A. J., Mjelde, R., Faleide, J. I., & Murai, Y. (2012). The eastern Jan Mayen microcontinent volcanic margin. *Geophysical Journal International*, *188*, 798–818. https://doi.org/10.1111/j.1365-246x.2011.05307.x

Breivik, A. J., Mjelde, R., Rai, A. K., & Frassetto, A. (2012). Geophyical survey of the Eggvin Bank and Logi Ridge-Greenland Sea. *Eos Trans. AGU*, *93*. Fall Meet. Suppl., Abstract T31B-2598.

Cammarano, F., & Guerri, M. (2017). Global thermal models of the lithosphere. *Geophysical Journal International*, *210*(1), 56–72.

Detrick, R., Collins, J., Stephen, R., & Swift, S. (1994). In situ evidence for the nature of the seismic layer 2/3 boundary in oceanic crust. *Nature*, *370*, 288–290.

Dilek, Y. (1998). Structure and tectonics of intermediate-spread oceanic crust drilled at DSDP/ODP holes 504B and 896A, Costa Rica Rift. In A. Cramp, et al. (Eds.), *Geological Evolution of Ocean Basin: Results from the Ocean Drilling Program* (Vol. 131, pp. 179–197): Geological Society, London, Special Publications.

Divins, D. L. (2004). Total sediment thickness of the world's oceans and marginal seas. World Data Cent. for Mar. Geol. and Geophys., Natl. Geophys. Data Cent., Boulder, Colo.

Doin, M. P., & Fleitout, L. (1996). Thermal evolution of the oceanic lithosphere: An alternative view. *Earth and Planetary Science Letters*, *142*(1-2), 121–136.

Elkins, L. J., Hamelin, C., Blichert-Toft, J., Scott, S. R., Sims, K. W. W., Yeo, I. A., et al. (2016). North Atlantic hotspot-ridge interaction near Jan Mayen Island. *Geochemical Perspectives Letters*, *2*, 55–67.

Elkins, L. J., Sims, K. W. W., Prytulak, J., Elliott, T., Mattielli, N., Blichert-Toft, J., et al. (2011). Understanding melt generation beneath the slow-spreading Kolbeinsey Ridge using ^{238}U, ^{230}Th, and ^{231}Pa excesses. *Geochimica et Cosmochimica Acta*, *75*, 6300–6329.

Fichtner, A., & Trampert, J. (2011). Resolution analysis in full waveform inversion. *Geophysical Journal International*, *187*(3), 1604–1624.

Förste, C., Schmidt, R., Stubenvoll, R., Flechtner, F., Meyer, U., König, R., et al. (2008). The GeoForschungsZentrum Potsdam/Groupe de Recherche de Geodesie Spatiale satellite-only and combined gravity field models: EIGEN-GL04S1 and EIGEN-GL04C. *Journal of Geodesy*, *82*(6), 331–346.

Funck, T., Geissler, W. H., Kimbell, G. S., Gradmann, S., Erlendsson, Ö., Kenneth, M., & Petersen, U. K. (2016). Moho and basement depth in the NE Atlantic Ocean based on seismic refraction data and receiver functions. *Geological Society, London, Special Publications*, *447*, 207–231. https://doi.org/10.1144/SP447.1

Furmall, A. V. (2010). Melt production and ridge geometry over the past 10 Myr on the southern Kolbeinsey Ridge, Iceland (Master's thesis), University of Oregon, USA.

Gaina, C., Gernigon, L., & Ball, P. (2009). Palaeocene—Recent plate boundaries in the NE Atlantic and the formation of the Jan Mayen microcontinent. *Journal of the Geological Society*, *166*, 601–616. https://doi.org/10.1144/0016-76492008-112

Gaina, C., Werner, S. C., Saltus, R., Maus, S., & GROUP, T. C.-G. (2011). Circum-Arctic mapping project: New magnetic and gravity anomaly maps of the Arctic. *Journal of the Geological Society*, *35*, 39–48.

Goes, S., & Van der Lee, S. (2002). Thermal structure of the north American uppermost mantle inferred from seismic tomography. *Journal of Geophysical Research*, *107*(B3), 2050. https://doi.org/10.1029/2000JB000049

Götze, H. J., & Lahmeyer, B. (1988). Application of three-dimensional interactive modeling in gravity and magnetics. *Geophyics*, *53*, 1096–1108.

Grose, C. J., & Afonso, J. C. (2013). Comprehensive plate models for the thermal evolution of oceanic lithosphere. *Geochemistry, Geophysics, Geosystems*, *14*, 3751–3778. https://doi.org/10.1002/ggge.20232

Haase, K. M., Devey, C. W., & Wieneke, M. (2003). Magmatic processes and mantle heterogeneity beneath the slow-spreading northern Kolbeinsey Ridge segment, North Atlantic. *Contributions to Mineralogy and Petrology*, *144*, 428–448.

Haase, C., Ebbing, J., & Funck, T. (2016). A 3D crustal model of the NE Atlantic based on seismic and gravity data. *Geological Society Special Publication*, *447*, 233–247.

Hermann, T. (2013). The Northeast Greenland margin-tectonic evolution (Ph.D. thesis), University of Jena.

Hermann, T., & Jokat, W. (2016). Crustal structure off Kong Oscar Fjord, east Greenland: Evidence for focused melt supply along the Jan Mayen Fracture Zone. *Tectonophysics*, *691*, 110–119.

Hooft, E. E. E., Brandsdóttir, B., Mjelde, R., Shimamura, H., & Murai, Y. (2006). Asymmetric plume ridge interaction around Iceland: The Kolbeinsey Ridge Iceland Seismic Experiment. *Geochemistry, Geophysics, Geosystems*, *7*, Q05015. https://doi.org/10.1029/2005GC001123

Howell, S. M., Ito, G., Breivik, A. J., Rai, A., Mjelde, R., Hanan, B., et al. (2014). The origin of the asymmetry in the Iceland hotspot along the Mid-Atlantic Ridge from continental breakup to present-day. *Earth and Planetary Science Letters*, *392*, 143–153.

Huck, H. (2012). *The road to open source: Sharing a ten years experience in building OpendTect, the open source seismic interpretation software*. Paper presented at the 74th EAGE Conference and Exhibition, Copenhagen, Denmark. https://doi.org/10.3997/2214-4609.20149897

Ito, G. (2001). Reykjanes "V"-shaped ridges originating from a pulsing and dehydrating mantle plume. *Nature*, *411*, 681–684.

Ito, G. T., & Lin, J. (1995). Mantle temperature anomalies along the past and paleoaxes of the Galápagos spreading center as inferred from gravity analyses. *Journal of Geophysical Research*, *100*(B3), 3733–3745.

Jacobson, R. S. (1992). Impact of crustal evolution on changes of the seismic properties of the uppermost oceanic crust. *Reviews of Geophysics*, *30*(1), 23–42.

Jakobsson, M., Mayer, L. A., Coakley, B., Dowdeswell, J. A., Forbes, S., Fridman, B., et al. (2012). International Bathymetric Chart of the Arctic Ocean (IBCAO) version 3.0. *Geophysical Research Letters*, *39*, L12609. https://doi.org/10.1029/2012GL052219

Jha, K., Parmentier, E. M., & Morgan, J. P. (1994). The role of mantle-depletion and melt-retention buoyancy in spreading-center segmentation. *Earth and Planetary Science Letters*, *125*(1-4), 221–234.

Jones, S. M., White, N., & Maclennan, J. (2002). V-shaped ridges around Iceland: Implications for spatial and temporal patterns of mantle convection. *Geochemistry, Geophysics, Geosystems*, *3*(10), 1059. https://doi.org/10.1029/2002GC000361

Kandilarov, A., Mjelde, R., Flueh, E., & Pedersen, R. B. (2015). V_p/V_s-ratios and anisotropy on the northern Jan Mayen Ridge, North Atlantic, determined from ocean bottom seismic data. *Polar Science*, *9*(3), 293–310.

Kandilarov, A., Mjelde, R., Pedersen, R. B., Hellevang, B., Papenberg, C., Petersen, C. J., et al. (2012). The northern boundary of the Jan Mayen Microcontinent, North Atlantic determined from ocean bottom seismic, multichannel seismic, and gravity data. *Marine Geophysical Researches*, *33*(1), 55–76.

Karato, S., & Jung, H. (1998). Water, partial melting and the origin of the seismic low velocity and high attenuation zone in the upper mantle. *Earth and Planetary Science Letters*, *157*, 193–207.

Kenyon, S., Forsberg, R., & Coakley, B. (2008). New gravity field for the Arctic. *Eos, Transactions American Geophysical Union*, *89*, 289–290.

Klingelhöfer, F., Géli, L., Matias, L., Steinsland, N., & Mohr, J. (2000). Crustal structure of a super-slow spreading centre: A seismic refraction study of Mohns Ridge, 72° N. *Geophysical Journal International*, *141*, 509–526.

Klingelhöfer, F., Géli, L., & White, R. S. (2000). Geophysical and geochemical constraints on crustal accretion at the very-slow spreading Mohns Ridge. *Geophysical Research Letters*, *27*(10), 1547–1550.

Kodaira, S., Mjelde, R., Gunnarsson, K., Shiobara, H., & Shimamura, H. (1998a). Structure of the Jan Mayen microcontinent and implication for its evolution. *Geophysical Journal International*, *132*, 383–400.

Kodaira, S., Mjelde, R., Gunnarsson, K., Shiobara, H., & Shimamura, H. (1998b). Evolution of oceanic crust on the Kolbeinsey Ridge, north of Iceland, over the past 22 Myr. *Terra Nova*, *10*, 27–31.

Kodaira, S., Mjelde, R., Shimamura, H., Gunnarsson, K., & Shiobara, H. (1997). Crustal structure of the Kolbeinsey Ridge, N. Atlantic, obtained by use of Ocean Bottom Seismographs. *Journal of Geophysical Research*, *102*(B2), 3131–3151.

Koptev, A., Cloetingh, S., Burov, E., François, T., & Gerya, T. (2017). Long-distance impact of Iceland plume on Norway's rifted margin. *Scientific Reports*, *7*, 10408.

Korenaga, J. (2008). Urey ratio and the structure and evolution of Earth's mantle. *Reviews of Geophysics*, *46*, RG2007. https://doi.org/10.1029/2007RG000241

Kroll, H., Kirfel, A., Heinemann, R., & Barbier, B. (2012). Volume thermal expansion and related thermophysical parameters in the Mg, Fe olivine solid-solution series. *European Journal of Mineralogy*, *24*(6), 935–956.

Laske, G., Masters, G., Ma, Z., & Pasyanos, M. (2013). Update on CRUST 1.0- A 1-degree Global Model of Earth's Crust. *Geophys. Res. Abstracts*, *15, abstract EGU2013-2658*.

Le Douaran, S., & Parsons, B. (1982). A note on the correction of ocean floor depths for sediment loading. *Journal of Geophysical Research*, *87*(B6), 4715–4722.

Marquart, G., Schmeling, H., & Čadek, O. (2007). Dynamic models for mantle flow and seismic anisotropy in the North Atlantic region and comparison with observations. *Geochemistry, Geophysics, Geosystems*, *8*, Q02008. https://doi.org/10.1029/2006GC001359

Meeßen, C., Sippel, J., Scheck-Wenderoth, M., Heine, C., & Strecker, M. R. (2018). Crustal structure of the Andean foreland in Northern Argentina: Results from data-integrative three-dimensional density modeling. *Journal of Geophysical Research: Solid Earth*, *123*, 1875–1903. https://doi.org/10.1002/2017JB014296

Mertz, D. F., Sharp, W. D., & Haase, K. M. (2004). Volcanism on the Eggvin Bank (Central Norwegian-Greenland Sea, latitude ~71°N): Age, source, and relationship to the Iceland and putative Jan Mayen plumes. *Journal of Geodynamics*, *38*, 57–83. https://doi.org/10.1016/j.jog.2004.03.003

Mjelde, R., Aurvåg, R., Kodaira, S., Shimamura, H., Gunnarsson, K., Nakanishi, A., & Shiobara, H. (2002). Vp/Vs-ratios from the central Kolbeinsey Ridge to the Jan Mayen Basin, North Atlantic; implications for lithology, porosity and present-day stress field. *Marine Geophysical Researches*, *23*(2), 123–145.

Mjelde, R., Eckhoff, I., Solbakken, S., Kodaira, S., Shimamura, H., Gunnarsson, K., et al. (2007). Gravity and S-wave modeling across the Jan Mayen Ridge, North Atlantic; implications for crustal lithology and continental break-up processes. *Marine Geophysical Researches*, *28*, 27–41. https://doi.org/10.1007/s11001-006-9012-3

Mjelde, R., Raum, T., Breivik, A. J., & Faleide, J. I. (2008). Crustal transect across the North Atlantic. *Marine Geophysical Researches*, *29*, 73–87. https://doi.org/10.1007/s11001-008-9046-9

Müller, R. D., Sdrolias, M., Gaina, C., & Roest, W. R. (2008). Age, spreading rates, and spreading asymmetry of the world's ocean crust. *Geochemistry, Geophysics, Geosystems*, *9*, Q04006. https://doi.org/10.1029/2007GC001743

Naif, S., Key, K., Constable, S., & Evans, R. L. (2013). Melt-rich channel observed at the lithosphere-asthenosphere boundary. *Nature*, *495*, 356–359. https://doi.org/10.1038/nature11939

National Geophysical Data Center (2006). *2-minute gridded global relief data (ETOPO2v2)*. Boulder, CO: National Geophysical Data Center. Retrieved from http://www.ngdc.noaa.gov/mgg/fliers/01mgg04.html

Nunns, A. (1982). The structure and evolution of the Jan Mayen Ridge and surrounding regions. In J. S. Watkins & C. L. Drake (Eds.), *Studies in Continental Margin Geology* (Vol. 34, pp. 193–208). Tulsa, Oklahoma, USA: Am. Assoc. Petrol. Geol.

Olesen, O., Ebbing, J., Lundin, E., Mauring, E., Skilbrei, J. R., Torsvik, T. H., et al. (2007). An improved tectonic model for the Eocene opening of the Norwegian-Greenland Sea: Use of modern magnetic data. *Marine and Petroleum Geology*, *24*, 53–66. https://doi.org/10.1016/j.marpetgeo.2006.10.008

Oxburgh, E. R., & Parmentier, E. M. (1977). Compositional and density stratification in oceanic lithosphere-causes and consequences. *Journal of the Geological Society London*, *133*(4), 343–355.

Parnell-Turner, R., White, N., Henstock, T., Murton, B., Maclennan, J., & Jones, S. M. (2014). A continuous 55-million-year record of transient mantle plume activity beneath Iceland. *Nature Geoscience*, *7*(12), 914–919.

Peron-Pinvidic, G., Gernigon, L., Gaina, C., & Ball, P. (2012a). Insights from the Jan Mayen system in the Norwegian-Greenland sea—I. Mapping of a microcontinent. *Geophysical Journal International*, *191*, 385–412.

Peron-Pinvidic, G., Gernigon, L., Gaina, C., & Ball, P. (2012b). Insights from the Jan Mayen system in the Norwegian-Greenland sea—II. Architecture of a microcontinent. *Geophysical Journal International*, *191*, 413–435.

Pilidou, S., Priestley, K., Debayle, E., & Gudmundsson, O. (2005). Rayleigh wave tomography in the North Atlantic: High resolution images of the Iceland, Azores and Eifel mantle plumes. *Lithos*, *79*, 453–474.

Priestley, K., & McKenzie, D. (2006). The thermal structure of the lithosphere from shear wave velocities. *Earth and Planetary Science Letters*, *244*, 285–301.

Priestley, K., & McKenzie, D. (2013). The relationship between shear wave velocity, temperature, attenuation and viscosity in the shallow part of the mantle. *Earth and Planetary Science Letters*, *381*, 78–91.

QGIS Devlopment Team (2009). QGIS geographic information system. Open Source Geospatial Foundation.

Rickers, F., Fichtner, A., & Trampert, J. (2013). The Iceland Jan Mayen plume system and its impact on mantle dynamics in the North Atlantic region: Evidence from full-waveform inversion. *Earth and Planetary Science Letters*, *367*, 39–51.

Ritsema, J., van Heist, H. J., & Woodhouse, J. H. (1999). Complex shear wave velocity structure imaged beneath Africa and Iceland. *Science*, *286*, 1925–1928.

Rychert, C. A., & Shearer, P. M. (2009). A global view of the lithosphere-asthenosphere boundary. *Science*, *324*(5926), 495–98.

Sandstå, R., Pedersen, N. R. B., Williams, R., Bering, D., Magnus, M., Sand, M., & Brekke, H. (2012). *Submarine fieldwork on the Jan Mayen Ridge: Integrated seismic and ROV-sampling*. Stavanger, Norway: Norwegian Petroleum Directorate. http://www.npd.no/Global/Norsk/3-Publikasjoner/Presentasjoner/Submarine-fieldwork-on-the-Jan-Mayen-Ridge-2012.pdf

Sandwell, D. T. (2001). *Cooling of the Oceanic Lithosphere and Ocean Floor Topography*. San Diego, CA, USA: University of California.

Schilling, J. (1999). Dispersion of the Jan Mayen and Iceland mantle plumes in the Arctic: A He-Pb-Nd-Sr isotope tracer study of basalts from the Kolbeinsey, Mohns, and Knipovich Ridges. *Journal of Geophysical Research*, *104*, 10,543–10,569.

Schmidt, S., & Götze, H. J. (1998). Interactive visualization and modification of 3-D models using GIS functions. *Physics and Chemistry of the Earth*, *23*, 289–296.

Schmidt, S., Plonka, C., Götze, H.-J., & Lahmeyer, B. (2011). Hybrid modelling of gravity, gravity gradients and magnetic fields. *Geophysical Prospecting*, *59*(6), 1046–1051.

Schoonman, C. M., White, N. J., & Pritchard, D. (2017). Radial viscous fingering of hot asthenosphere within the Icelandic plume beneath the North Atlantic Ocean. *Earth and Planetary Science Letters*, *468*, 51–61.

Schutt, D. L., & Lesher, C. E. (2006). Effects of melt depletion on the density and seismic velocity of garnet and spinel Iherzolite. *Journal of Geophysical Research*, *111*, 401. https://doi.org/10.1029/2003JB002950

Scott, D. R., & Stevenson, D. (1989). A self-consistent model of melting, magma migration and buoyancy-driven circulation beneath mid-ocean ridges. *Journal of Geophysical Research*, *94*(B3), 2973–2988.

Shorttle, O., Maclennan, J., & Jones, S. M. (2010). Control of the symmetry of plume-ridge interaction by spreading ridge geometry. *Geochemistry, Geophysics, Geosystems*, *11*, Q0AC05. https://doi.org/10.1029/2009GC002986

Sleep, N. H. (1997). Lateral flow and ponding of starting plume material. *Journal of Geophysical Research*, *102*(B5), 10,001–10,012.

Stein, C. A., & Stein, S. (1992). A model for the global variation in oceanic depth and heat flow with lithospheric age. *Nature*, *359*, 123–129.

Stixrude, L., & Lithgow-Bertelloni, C. (2005). Mineralogy and elasticity of the oceanic upper mantle: Origin of the low-velocity zone. *Journal of Geophysical Research*, *110*, B03204. https://doi.org/10.1029/2004JB002965

Tan, P., Breivik, A. J., Trønnes, R. G., Mjelde, R., Azuma, R., & Eide, S. (2017). Crustal structure and origin of the Eggvin Bank west of Jan Mayen, NE Atlantic. *Journal of Geophysical Research: Solid Earth*, *122*, 43–62. https://doi.org/10.1002/2016JB013495

Thiede, J., & Hempel, G. (1991). *Die Expedition ARKTIS-VII/1 mit FS "Polarstern" 1990, Reports on Polar and Marine Research* (Vol. 80, pp. 1–137). Bremerhaven: Alfred Wegener Institute for Polar and Marine Research.

Trønnes, R. G., Planke, S., Sundvoll, B., & Imsland, P. (1999). Recent volcanic rocks from Jan Mayen: Low-degree melt fractions of enriched northeast Atlantic mantle. *Journal of Geophysical Research*, *104*(B4), 7153–7168.

Uieda, L., & Barbosa, V. C. F. (2011). *3D gravity inversion by planting anomalous densities*. Paper presented at the Twelfth International Congress of the Brazillian Geophysical Society, Rio de Janeiro, Brazil. https://doi.org/10.1190/sbgf2011-179

Uieda, L., Oliveira, V. C. Jr, & Barbosa, V. C. F. (2013). Modeling the Earth with fatiando a terra. In *Proceedings of the 12th Python in Science Conference (SciPy 2013)* (pp. 96–103). Austin, TX.

Voss, M., & Jokat, W. (2007). Continent-ocean transition and voluminous magmatic underplating derived from P-wave velocity of the East Greenland continental margin. *Geophysical Journal International*, *170*, 580–604. https://doi.org/10.1111/j.1365-246x.2007.03438.x

Weigel, W., Flüh, E. R., Miller, H., Butzke, A., Dehghani, G. A., Gebhardt, V., et al. (1995). Investigations of the East Greenland continental margin between 70° and 72° N by deep seismic sounding and gravity studies. *Marine Geophysical*, *17*, 167–199.

White, R. S., Bown, J. W., & Smallwood, J. R. (1995). The temperature of the Iceland plume and origin of outward-propagating V-shaped ridges. *Journal of the Geological Society*, *152*, 1039–1045.

Xue, M., & Allen, R. M. (2005). Asthenospheric channeling of the Icelandic upwelling: Evidence from seismic anisotropy. *Earth and Planetary Science Letters*, *235*, 167–182.

Zhang, Y., & Lay, T. (1999). Evolution of oceanic upper mantle structure. *Physics of the Earth and Planetary Interiors*, *114*, 71–80.